

ABSTRACT

ANGUS, MICHAEL PETER. The Effect of Asymmetrical Topography on the Generation of Internal Waves. (Under the direction of Dr. Ping-Tung Shaw.)

Internal wave generation over steep topography, such as a ridge or sill, is a well observed phenomenon in the ocean. In this study, internal waves in idealized oceanographic settings are generated by barotropic tidal flow over a two-dimensional ridge, using a nonhydrostatic numerical model. A series of experiments are performed in which internal waves are generated on topography with a steep slope on one side, while the other slope varies in gradient. The impact of bottom topography shape on wave generation is examined. The results show that the response changes greatly depending on the steepness of the varying slope. If the varying slope is subcritical, internal wave energy flux is a minimum, despite the fixed slope being critical. The energy flux increases with increasing slope if the slope is near critical. Further increases in slope gradient produce a maximum in energy flux. The side of the domain on which the topography is steepest always experiences the highest energy flux. The Mascarene Plateau in the western Indian Ocean is examined in this context. The Mascarene Plateau is asymmetrical with a steeper slope on the west side. The slightly larger intensity of internal waves on the west side of the Mascarene plateau agrees with the asymmetrical ridge topography. The surface currents and latitude are found to be of lesser impact on the generation of internal waves than the change in topographical slope.

The Effect of Asymmetrical Topography on the Generation of Internal Waves

by
Michael Angus

A thesis submitted to the Graduate Faculty of
North Carolina State University
in partial fulfillment of the
requirements for the Degree of
Master of Science

Marine Earth and Atmospheric Sciences

Raleigh, North Carolina

2012

APPROVED BY:

Dr Alberto Scotti

Dr Ruoying He

Dr Ping-Tung Shaw

Chair of Advisory Committee

Biography

Michael Angus was born on April 17th 1988, in the idyllic North East of England, a region few people ever choose to leave. After finishing school, Michael did however venture out into the world to begin his B.Sc in Meteorology and Oceanography from the University of East Anglia in 2006. During his studies, he completed a yearlong work experience program at the National Oceanography Centre in Liverpool. On graduating, Michael moved even further afield to join North Carolina State University in 2010. Here he expects to complete his M.S. degree in 2012 and will continue to pursue a Ph.D degree.

Acknowledgements

The initial funding for the project was provided by the ONR (Office of Naval Research) and I would like to thank them for their support. I would like to thank my adviser Dr Ping-Tung Shaw for his helpful suggestions and professional instruction throughout this masters project as well as the other members of my advisory committee for agreeing to serve and advise this project: Dr Alberto Scotti and Dr Ruoying He. On a personal note, I am extremely grateful for, and continually amazed at, the patience and support of Rowan Argent. Finally, I would like to thank my Parents, without whom I would quite literally not be here.

Table of Contents

List of Tables	v
List of Figures	vi
1. Introduction	1
1.1 Background.....	1
1.2 The Mascarene Plateau case study	5
1.3 Internal wave energy flux.....	7
2. Model description and experiments.....	11
2.1 Model setup	11
2.2 Experiment parameters.....	14
2.3 Ridge design and experimental setup	16
3. Model results	18
3.1 Normalized energy flux	18
3.2 Internal wave energy.....	19
3.3 Baroclinic energy flux	22
3.4 Additional experiments.....	26
3.4.1 Plateau width.....	26
3.4.2 Steady current	28
3.4.3 Latitude.....	29
4. Mascarene Plateau	30
4.1 Model results.....	30
4.2 Mode 2 waves	32
5. Discussion	33
6. Conclusion	37
REFERENCES.....	39

List of Tables

Table 2.1 List of experiments.....44

Table 2.2 List of secondary parameter experiments.....45

List of Figures

Figure 1.1	Internal wave propagation in the temperature field. Wave propagates from left to right at the western Portuguese mid-shelf, with the leading edge on the far right (adapted from Quaresma et al. 2007).....	46
Figure 1.2	Map of recognized internal wave locations (adapted from Jackson, 2004).....	47
Figure 1.3	Satellite image of surface modulations caused by internal waves at the Straits of Gibraltar from http://envisat.esa.int/handbooks/asar/CNTR1-1-5.html	48
Figure 1.4	Map of the Mascarene Plateau from da Silva et al. (2011). The source region of the internal waves between the two shallow water banks is highlighted. Grey regions represent areas shallower than 1000m and dark regions represent land.....	49
Figure 1.5	Surface currents at the Mascarene Plateau, adapted from New et al. (2007).....	50
Figure 1.6	Topography of the Mascarene Plateau, a) in plan view (new et al. 2007) and b) in profile (Konyaev 1995). The depth contours in a) are in meters.....	51
Figure 2.1	Current profile used in the numerical study. The value of U_m is 10 cm s^{-1} at the surface and decreases exponentially with depth.....	52
Figure 2.2	(a) Density ρ_a in kg m^{-3} and buoyancy frequency N in rad s^{-1} in all experiments listed in tables 2.1 and 2.2. The corresponding normal modes are shown (b) for horizontal velocity and (c) for density perturbation. The phase speeds are 1.52, 0.64, and 0.41 m s^{-1} for the first three modes. From Shaw et al. (2009).....	53
Figure 2.3	Study area A, enclosed in a dotted line on a baroclinic energy flux plot in the x-t plane. The Contour interval is 1000 (W/m).....	54
Figure 2.4	The model configuration. Contours show the background density field averaged over 12 hours for case 1D. The model is forced by a semidiurnal tide.....	55
Figure 3.1	Normalized energy flux as a function of slope parameter, for all cases. The subcritical and critical ranges of γ are enclosed by a rectangle and an oval respectively. The energy levels for the end members of the experiment series (1A and 1M) are plotted as black dotted lines.....	56

Figure 3.2	Internal wave energy density (J/m^3) averaged over one tidal cycle 49.70 – 62.10 hours, for L equal to (a) 0 km (b) 12 km and (c) 18 km. The width of the slope on the left is 15 km. The contour interval in all panels is 1 J/m^3	57
Figure 3.3	Same as Figure 3.2 but for L equal to (a) 38 km (b) 78 km and (c) infinity. The contour interval in the top two panels is 1 J/m^3 and 0.1 J/m^3 in the bottom panel.....	58
Figure 3.4	Vertically integrated horizontal energy flux (W/m) as a function of x for the supercritical experiments 1A, 1B, 1C and 1D. The flux is averaged over the tidal cycle 49.68 – 62.10 hours. The ridge is centered at $x=0 \text{ km}$	59
Figure 3.5	Vertically integrated horizontal energy flux (W/m) as a function of x for the transitional experiments 1E, 1F, 1G, 1H and 1I. The flux is averaged over the tidal cycle 49.68 – 62.10 hours. The ridge is located at $x=0 \text{ km}$	60
Figure 3.6	Vertically integrated horizontal energy flux (W/m) as a function of x for the subcritical experiments 1J, 1K, 1L and 1M. The flux is averaged over the tidal cycle 49.68 – 62.10 hours. The ridge is located at $x=0 \text{ km}$	61
Figure 3.7	Internal wave energy density (J/m^3) for (a) 1D and (b) 2A averaged over one tidal cycle, 49.70 – 62.10 hours. The contour interval is 1 J/m^3	62
Figure 3.8	Vertically integrated horizontal energy flux (W/m) as a function of x for experiments 1D and 2A The flux is averaged over the tidal cycle 61.06 – 72.48 hours. The ridge is located at $x=0 \text{ km}$	63
Figure 3.9	Internal wave energy (J/m^3) for (a) 2B (b) 1D and (c) 2C. The energy density is averaged over one tidal cycle, between 49.68 – 62.10 hours. The contour interval is 1 J/m^3	64
Figure 3.10	Vertically integrated horizontal energy flux (W/m) as a function of x for 1D forced by three different tidal currents. The flux is averaged over the tidal cycle 49.68 – 62.10 hours. The ridge is located at $x=0 \text{ km}$	65
Figure 3.11	Vertically integrated horizontal energy flux (W/m) as a function of x at four different latitudes. The flux is averaged over the tidal cycle 49.68 – 62.10 hours. The ridge is located at $x=0 \text{ km}$	66
Figure 4.1	Contour plots of baroclinic velocity u in experiment 1G, at $t=52.78 \text{ hours}$ with increments every 3 hours. The barotropic tidal flow is at a maximum in the first and third panels (right and left respectively) and is zero in the second and fourth panels. The contour interval is 0.01 m/s^{-1}	67

Figure 4.2 Internal wave energy density (J/m^3) for the Mascarene Plateau experiment 1G. Averaged over one tidal cycle, 48.65 – 60.97 hours. The contour interval is 0.5 J/m^3	68
Figure 4.3. Vertically integrated energy flux in the x-t plane for the Mascarene plateau experiment 1G. Contour interval is 1000 (W/m)	69
Figure 4.4. Vertically integrated energy flux in the x-t plane for experiment 1A, with a steep topography on the right side. Mode two waves are observed between $t=55$ and 70 hours in the region $x=0$ and 100 km . Contour interval is 750 (W/m)	70

1. Introduction

1.1 Background

A tidal flow, forced over shallow topographic features in a stratified ocean, can produce internal waves of tidal frequencies. In the case of a shallow thermocline in the upper ocean, wave amplitude may increase greatly (*Shaw et al.*, 2009), forming an internal solitary wave (ISW) at the interface between layers of differing water density (the pycnocline). ISWs are observed across the oceans, frequently along continental margins, sills and ridges. A wave packet of ISWs is usually characterized by a steep front with large temperature gradients, strong surface convergence, and a strong downward flow at the leading edge, followed by trailing waves of shorter wavelengths. A vertical cross section of ISW structure is presented in **Figure 1.1**.

A comprehensive list of ISW observation sites has been compiled by *Jackson* (2004), with major study sites including the South China Sea (SCS) (*Lien et al.*, 2005; *Shaw et al.*, 2009; *Ramp et al.*, 2004; *Ramp et al.*, 2010), Massachusetts Bay (*Scotti et al.*, 2007) and the Mascarene Plateau (*da Silva et al.*, 2011) amongst others. **Figure 1.2** provides a map of currently recognized ISW locations. Observations of internal waves increase during the summer months (*Zheng et al.*, 2007). This is most likely due to seasonal variation in the

presence of a shallow thermocline (*Shaw et al.*, 2009) and large scale surface currents, such as the Kuroshio in the SCS region.

Given the large amplitude and geographical range of ISWs in the oceans, it is unsurprising that their consequences are equally wide ranging. Physically, ISWs have been proposed as a mechanism for large scale sheer turbulence in the surface layer (*Moum et al.*, 2003), and as a significant contributor to ocean heat fluxes (*Shroyer et al.*, 2010). Geologically, *Pomar et al.* (2012) recently found that these waves can induce mobilization of bottom sediments through strong bottom-current pulses by reviewing the global impact of ISWs on the sediment record. Additionally, *Reeder et al.* (2011) implicate ISWs as the primary cause of sediment bottom ripples in the South China Sea. ISWs also have a role to play in the transport of nutrients; Pilot Whales have been known to follow in the wake of ISWs (*Moore and Lien*, 2007), and vertical fish migration following ISWs was recently observed off the coast of Namibia (*Kaartvedt et al.*, 2012).

Synthetic Aperture Radar (SAR) images provide evidence for the existence of ISWs, which are observed as dark bands or ripples on the ocean surface (*Cacchione and Pratson*, 2004). An example of the surface “slicks” or “bands” generated by an internal wave at the Straits of Gibraltar is shown in **Figure 1.3**. These disturbances are caused by the modulating effect

of convergence and divergence on surface roughness, in near-surface currents (*da Silva et al.*, 2011).

Numerous studies have applied statistical and observational methods to study ISWs in remote sensing images. The technique was first pioneered by *Apel* (1975) who compared the period of internal waves from direct cruise measurements in the New York Bight to the period observed in surface modulation, and found good agreement between the two. In the SCS, *Zheng et al.* (2007) used SAR images for a statistical analysis of internal wave occurrence. Their study indicated interannual variability with higher frequencies of wave occurrence from April to July, peaking in June. Based on temperature measurements in the region, the authors found that the wave variability was associated with a shallower thermocline in the summer months. They suggested that thermocline shoaling is an important factor in ISW generation. The higher frequency of surface modulations in the summer is therefore caused by the increased number of ISWs, which are more easily visible than internal waves. A full summary of internal wave remote sensing studies was recently conducted by *Klemas* (2012), illustrating that the physical parameters (wave speed, propagation direction etc.) available in SAR images can be used in theoretical studies to derive important physical information.

Theoretical studies of solitary waves are nothing new; In 1895 *Korteweg and de Vries* first derived the mathematical properties of a “soliton”, for surface waves (*Konyaev et al.*, 1995). Further analytical solutions were derived by *Lee and Beardsley* (1974) and *Hibiya* (1986) using the Boussinesq approximations; *Hibiya* (1986) is the basis for the numerical model used in this study (*Shaw and Chao*, 2006). Numerical models, such as the Regional Ocean Model system used by *Buijsman et al.* (2010), are now frequently utilized to investigate internal wave properties. In addition, the SCS has been particularly well studied using process orientated models. *Chao et al.* (2007) examined the role of topographic height on westward propagation of internal tides, predicting that the topography in the region was capable of producing ISWs, as observed by *Zhang et al.* (2007). *Shaw et al.* (2009) discussed the role of thermocline shoaling on ISW generation, a primary reason for internal waves being more commonly observed to the west of the ridge in the SCS.

Two mechanisms of ISW generation over a ridge have been hypothesized: lee wave generation and internal tide generation. In lee wave generation, a depression in the thermocline is first produced in the lee of a ridge by the barotropic tidal flow (*Maxworthy*, 1979). As the tide reverses, the depression moves away from the ridge in the direction of the flow to form a rank ordered solitary wave packet. In internal tide generation, fronts

develop in large-amplitude internal tides produced by flow over a ridge. Wave packets then form at the wavefronts by nonlinear dispersion (*Lee and Beardsley, 1974*).

1.2 The Mascarene Plateau case study

Situated just to the east of Madagascar at 20°S 60°E, the Mascarene Plateau is comprised of an extensive range of banks and Islands (**Figure 1.4**), stretching approximately 2000 km. The South Equatorial Current (SEC), the major current in the South Indian Ocean, flows over the plateau almost entirely between the Saya de Malha and Nazareth banks (*New et al., 2007*). The flow direction here is predominately to the west (**Figure 1.5**) with speeds of around 50-70 cm s^{-1} in the well mixed surface layer (depth of 50 – 100m). Tidal currents in the region can reach 35 cm s^{-1} with individual M_2 and S_2 components typically around 15 cm s^{-1} (*da Silva et al., 2011*). From previous studies (*Konyaev et al., 1995; New et al., 2007*), the bottom topography between the two banks consists of a ridge with a steep west slope and a gentle, shallower east slope (**Figure 1.6**).

Utilizing SAR images, *da Silva et al. (2011)* examined ISWs emanating from the Mascarene Plateau. By mapping the distribution of surface disturbances, the study found the average phase speed (2.98 m/s to the west 2.38 m/s to the east), wavelength (typically >5km for the leading wave) and along crest length (approx. 300 km) of the ISWs. The maximum distance that the internal waves can reach is typically 400 km to the west of the sill and 250 km to

the east, with a period corresponding to the semi-diurnal tidal cycle (12.42 hours). This result confirmed the findings of *Morozov et al.* (2009), that the temperature and currents fluctuated at the M_2 tidal frequency. The shallow sill between the two banks is suggested by *da Silva et al.* (2011) as the primary generation site of the ISWs, based on tracing the surface disturbances to their point of origin.

The presence of internal waves at the Mascarene Plateau has been confirmed observationally by measuring thermocline displacement in the region (*Konyaev et al.*, 1995). Using the temperature data collected along ship tracks across the ridge in March 1987 (*Morozov and Vlasenko*, 1996), *Konyaev et al.* (1995) concluded that internal waves appeared on both sides of the sill, and hypothesized two possible scenarios for their generation: (1) a hydraulic jump on the west side of the ridge, or (2) by the internal tide mechanism. In the first scenario, the combination of westward current (SEC) and maximum westward tidal flow result in a lee wave forming semi-diurnally. It is argued that the presence of the SEC prevents a lee wave forming on the eastern side of the ridge. The study did not suggest which scenario was more likely in the region. Recently *da Silva et al.* (2011) favored scenario one based on an analysis of the timing and location of the wave packets. Both *da Silva et al.* (2011) and *Konyaev et al.* (1995) agreed that the westward waves are more energetic than their eastward counterparts and concluded that this phenomenon was

due to the predominantly westward SEC. This also explains the increase in phase speed and maximum distance to the west of the sill as observed by *da Silva et al.* (2011).

In addition to the observed mode 1 waves generated at the ridge, *Vlasenko and Morozov* (1993) noted the existence of several other modes generated in the slope region when comparing numerical simulations with ADCP data. The authors concluded that at some distance from the ridge, the higher modes dissipate and the entire depth of the ocean is subjected only to first-mode oscillations. *Konyaev et al.* (1995) commented on the existence of mode 2 waves, suggesting they did not survive crossing the sill. *Da Silva et al.* (2011) found evidence for the existence of mode 2 waves, travelling eastward at a phase speed approximately 0.4 ms^{-1} in both the SAR images and thermocline displacement from temperature records.

1.3 Internal wave energy flux

As a tidal current passes over topography, energy is converted into either turbulent mixing or internal waves. The baroclinic energy flux F associated with the internal wave generated in an ocean of infinite depth with small bottom slope was first solved by *Bell* (1975) and has been used in numerous theoretical studies since (*Balmforth et al.*, 2002; *Smith and Young*,

2003; *Qian et al.*, 2010). In this study, the energy flux will be described in terms of the nondimensional slope parameter:

$$\gamma = h_x / \alpha \quad (1)$$

where h_x is the maximum slope of the topography and α is the slope of the internal wave beam (*Garrett and Kunze*, 2007). From linear wave theory, for waves of frequency ω , the slope of the wave beam can be defined as:

$$\alpha = \left[(\omega^2 - f^2) / (N^2 - \omega^2) \right]^{1/2} \quad (2)$$

where N is the buoyancy frequency and f is the Coriolis parameter. The slope parameter (γ) can be defined as either supercritical ($\gamma > 1$) or subcritical ($\gamma < 1$). Bell's solution (1975) for energy flux in an ocean of infinite depth is in the range $\gamma \ll 1$ and is given by:

$$F \propto \rho_0 U_0^2 h_0^2 (N^2 - \omega^2)^{1/2} (1 - f^2 / \omega^2)^{1/2} \quad (3)$$

Where ρ_0 is a reference density, h_0 is the topographic height and U_0 is the amplitude of the tidal current. Although equation (3) is independent of the ridge slope (*Smith and Young*, 2003), several studies have confirmed the relationship between F and γ in this limit (*Balmforth et al.*, 2002; *Khaliwala*, 2003; *St. Laurent et al.*, 2003).

In a series of experiments between the interval $0 < \gamma < 1$, *Balmforth et al. (2002)* show that enhancement in energy flux above Bell's prediction followed a smooth and modest increase, up to 14% larger for a gaussian bump as the slope parameter approaches 1. *Petrelis et al. (2006)* approximated the case in the supercritical range $\gamma > 1$ using knife-edge topography, in which the width of the ridge tends to 0 for a given height and $\gamma \rightarrow \infty$ (see *Peacock et al., 2008*). Their solution provided a rough estimate for more realistic supercritical ridges. They concluded that the radiative power of an internal wave increases monotonically with increasing slope parameter in the supercritical range. A recent laboratory study by *Dossmann et al. (2011)* confirmed the validity of this trend, showing good agreement with energy flux values over a supercritical gaussian ridge calculated theoretically and numerically (such as *St. Laurent et al., 2003*).

The relationship between F and γ highlights the importance of ridge topography on the generation of internal waves. Examining the Strait of Messina case study, *Brandt et al. (1997)* observed southward propagating internal waves more frequently than northward propagating internal waves concluding that this asymmetry is the result of the north-south asymmetry of the topography of the strait of Messina. This implies that the steeper west slope at the Mascarene Plateau may have an impact on the internal wave field. The key questions are then: are the more frequent westward travelling internal waves observed at

the Mascarene Plateau caused by the asymmetry of the topography, the mean surface current (*New et al.*, 2007), or a combination of these factors? To what extent is one more important than the other?

Using a non-hydrostatic model, this study intends to replicate ISW generation over a series of two-dimensional ridges. While one slope remains supercritical, the other slope will cover both the subcritical and supercritical ranges. The contribution to the ISW energy flux from both sides of the topography is calculated to examine the role of asymmetrical ridge topography on ISW generation worldwide. The Mascarene Plateau is considered as a case study in this context, and surface currents are examined as an alternative hypothesis for the observed asymmetry in ISW occurrence.

This thesis is organized as follows: Chapter 2 describes the model configuration and the experiment setup. Chapter 3 presents the model results for a variety of topographical slopes ranging from a step function ($\gamma \rightarrow \infty$) to a continental shelf ($\gamma \rightarrow 0$). Chapter 4 examines the Mascarene Plateau topography case study in more detail. Chapter 5 and 6 are discussion and conclusions.

2. Model description and experiments

2.1 Model Setup

For this study, the three-dimensional nonhydrostatic numerical model of *Shaw and Chao* (2006) is used, also previously employed in *Chao et al* (2007), *Shaw et al.* (2009) and *Qian et al.* (2010). The model solves the three-dimensional momentum, continuity, and density equations with Boussinesq and rigid-lid approximations. The governing equations are:

$$\frac{D\mathbf{u}}{Dt} + 2\Omega\mathbf{k}' \times \mathbf{u} = -\frac{1}{\rho_0} \nabla p - \frac{\rho}{\rho_0} g\mathbf{k} + A_H \nabla_H^2 \mathbf{u} + \nu \frac{\partial^2 \mathbf{u}}{\partial z^2} \quad (4)$$

$$\nabla \cdot \mathbf{u} = 0 \quad (5)$$

$$\frac{D\rho}{Dt} = K_H \nabla_H^2 \rho + \kappa \frac{\partial^2 \rho}{\partial z^2} \quad (6)$$

where \mathbf{u} is the three-dimensional velocity vector (u, v, w) in the (x, y, z) coordinates, \mathbf{k}' is a unit vector pointing upward from the North Pole, \mathbf{k} is the local upward unit vector, ρ is the deviation of density from a reference density ρ_0 (1028 kg m^{-3}), Ω is the Earth's rotation rate, and p is the pressure. The kinematic eddy viscosity and diffusivity are constant, so that $A_H = 10^6 \text{ m}^2/\text{s}$, $K_H = 10^5 \text{ m}^2\text{s}^{-1}$, $\nu = 1 \times 10^{-4} \text{ m}^2\text{s}^{-1}$, and $\kappa = 0.1 \times 10^{-4} \text{ m}^2\text{s}^{-1}$. Equation (5) includes both the horizontal and vertical components of the Coriolis acceleration. The finite

difference form of the governing equations and the solution procedure are described in detail in *Shaw and Chao (2006)*.

The model domain is from $x = -300$ km to 300 km in the east-west direction and from $z = -H = -800$ m at the bottom to 0 m at the surface. The horizontal and vertical grid sizes are 200 m and 10 m respectively. A rigid lid is used at the surface for computational efficiency which, due to the relatively small phase speed of baroclinic waves compared to that of the barotropic waves, should not affect the amplitude of internal waves over the ridge significantly. In the y direction, two grid cells are used with a periodic boundary condition; no y -variation is introduced, so that although the model is three-dimensional, this study is in the two dimensional x and z space.

Flow over the ridge is forced by the oscillating barotropic M_2 tide and a steady current (U_c).

The velocity in the x -direction is given by:

$$U = U_c + U_0 \sin \omega t \quad (7)$$

where $\omega = 2\pi/12.42 \text{ rad hr}^{-1} = 8.86 \times 10^{-4} \text{ rad s}^{-1}$ is the tidal frequency. For this study, $U_0 = 10 \text{ cm s}^{-1}$. The barotropic tidal current, which starts from zero at $t=0$ is initially eastward.

The steady current U_c is represented either as a mean flow, constant with depth, or as a surface current decaying exponentially with depth:

$$U_c = U_m e^{(z/d)} \quad (8)$$

where U_m is the mean surface current and $d = 50$ m is the e-folding depth (**Figure 2.1**).

The perturbation density ρ' is

$$\rho'(x, z, t) = \rho - \rho_a(z) \quad (9)$$

The ambient stratification $\rho_a(z)$ is given by

$$\rho_a(z) = -\frac{\Delta\rho}{2} \left[1 + \tanh\left(\frac{z-z_0}{D}\right) \right] \quad (10)$$

where $\Delta\rho$ is the scale of density perturbation. The thermocline is centered at depth $z_0 (= -50$ m) with thickness $D (= 120$ m). The buoyancy frequency derived from (10) is

$$N = \left[-(g/\rho_0) d\rho_a/dz \right]^{1/2} = \left(\frac{g\Delta\rho}{2\rho_0 D} \right)^{1/2} \text{sech}\left(\frac{z-z_0}{D}\right) = N_{\max} \text{sech}\left(\frac{z-z_0}{D}\right). \quad (11)$$

The maximum buoyancy frequency N_{\max} occurs at $z = z_0$, and $N_{\max} = N_0 = 0.015$ rad/s for

$\Delta\rho = 6$ kg/m³ and $\rho_0 = 1028$ kg/m³. **Figure 2.2** shows the modal decomposition for this

stratification. Mode-1 waves associated with (11) have zero horizontal velocity and

maximum vertical velocity at $z = -200$ m.

The phase speed of the mode-1 wave is 1.52 ms^{-1} for $N_{\text{max}} = N_0$, and is proportional to N_{max} in other experiments. For semidiurnal tides, the internal wave energy is negligible below $z = -700 \text{ m}$. Extending the depth of the model to below 800m should not therefore affect internal wave generation significantly.

2.2 Experiment parameters

In this study, ISWs will be described in terms of both their overall energy (E) and normalized energy flux (F'). The baroclinic velocity $\mathbf{u}' \equiv (u', v', w')$, calculated by subtracting the depth-averaged horizontal velocity from the total velocity \mathbf{u} , is used in the equation for the perturbation kinetic energy density:

$$K = \frac{1}{2} \rho_0 (u'^2 + v'^2 + w'^2) \quad (12)$$

and the perturbation potential energy density is

$$P = \frac{1}{2} \frac{g^2 \rho'^2}{\rho_0 N^2} \quad (13)$$

The total energy E is then the sum of (12) and (13).

The internal wave energy flux is $p'\mathbf{u}'$, where p' is the perturbation pressure. From *Nash et al.* (2005) p' is obtained by subtracting the depth-averaged pressure \bar{p} from hydrostatic pressure p :

$$p'(x, z, t) = p(x, z, t) - \bar{p}(x, t) \quad (14)$$

where the depth averaged pressure is given by

$$\bar{p} = \frac{1}{|z_b|} \int_{z_b}^0 dz \left(\int_z^0 p'(x, z', t) g dz' \right) \quad (15)$$

where z_b is the z -coordinate for the bottom.

In this study, the vertically integrated horizontal energy flux given by

$$I = \int_{z_b}^0 \rho' \mathbf{u}' dz \quad (16)$$

is averaged over an area A , following a wave beam in time and space (**Figure 2.3**). The spacial average of A is one wavelength in the x -direction (67.96km) and the temporal average is one wave period (12.42 hours). The wavelength is calculated using the theoretical phase speed of the internal wave, 1.52 ms^{-1} . The baroclinic energy flux is calculated

$$F = \overline{I(A)} \quad (17)$$

where the overbar represents averaging over A .

Qian et al. (2010) showed that a normalization scheme may be applied to F . The nondimensional horizontal energy flux (F') is defined as

$$F' = \frac{F}{\rho H U_0 \bar{N}_r h_0} \quad (18)$$

Where \bar{N}_r is the averaged buoyancy frequency over the depths of the ridge h_0

$$\bar{N}_r = \frac{1}{h_0} \int_{-z_b}^{-z_b+h_0} N dz \quad (19)$$

2.3 Ridge design and experimental setup

The tidal flow over idealized topography, described in Eq. (7), forms the basis for a series of experiments. Each experiment consists of a fixed slope on the west side of the ridge, a plateau width of 20 km, and a variable east slope. The ridge is described by the Witch-of-Agnesi function

$$h(x) = h_m / \left[1 + (x/L)^2 \right] \quad (20)$$

where h_m is the maximum height, and L is the half-width of the slope. In this study, h_m is fixed at 600 m, and L is varied to change the maximum slope of the ridge on the east side, while being fixed at $L=15$ km on the west side.

The maximum slope, $h'_x = (3^{3/2}/8)h_m/L$, is at $x = 3^{-1/2}L$. The ridge is shifted vertically for different ridge heights h_0 , measured from the bottom ($z = -800$ m) to the ridge crest. The

slope of the ridge does not change with the vertical shift. The model setup is shown in **Figure 2.4**. Each experiment in **Table 2.1** varies in L only on the east (right) side of the ridge. For example, experiment 1D corresponds to a ridge of $L = 15$ km for the east slope. The experiment 1G is based on the Mascarene Plateau, following the measurements of the local topography by *New et al. (2007)*. An additional set of experiments, detailed in **Table 2.2** are used to examine other potential impacts on internal wave generation, explicitly the latitude of the ridge location, the plateau width and the surface current velocity.

In this study, the wave slope in eq. (1) is represented by the average wave slope between $z_t = -200$ m and 0 m

$$\alpha = \frac{1}{|z_t|} \int_{z_t}^0 \left(\frac{\omega^2 - f^2}{N^2 - f^2} \right)^{\frac{1}{2}} dz \quad (21)$$

The maximum ridge slope h'_x is used for h_x . **Table 2.1** provides a list of the slope parameter (γ) and the slope width (L) for all experiments.

3. Model Results

3.1 Normalized energy flux

The normalized baroclinic energy flux, F' is calculated on both sides of the ridge as described by eq(16) – (18) and shown in **Figure 3.1**. For all cases, the wave energy flux is slightly higher on the side of the ridge with a steeper slope, with the approximately equal symmetrical case (1D, $\gamma=2.36$) being the only exception to this. Over the whole range of experiments, F' increases substantially with the slope parameter for the east slope. Three separate categories are defined: subcritical, transitional and supercritical.

In the subcritical range $\gamma < 0.75$ (1J, 1K and 1M, enclosed by a rectangular box), the flux is at a minimum value on both sides of the topography, $F' \approx 0.2$. There is no significant difference observable between the cases in this range. However, energy flux in the westward propagating waves is consistently higher than in the eastward propagating waves. In the transitional range $0.75 \leq \gamma \leq 2$, the wave flux increases with the east slope parameter γ . Although the westward flux continues to be higher than the eastward flux, the difference between the two decreases in this range, as the east and west slopes become similar. In the supercritical range $\gamma > 2$, the westward energy flux of the internal wave does not vary with increasing east slope parameter, and reaches an approximately constant value of 0.8. The eastward wave energy flux continues to increase slowly, as the east slope becomes steeper

than the west slope. The cases in this range (1D, 1C, 1B) are enclosed in an ellipse and like the subcritical cases, have similar characteristics. The value of F' for eastward propagating waves of the two end member cases (1A and 1M) are shown as two black horizontal lines, bounding the supercritical and subcritical regions. These two cases do not share the properties of the conventional topography cases, as will be discussed in due course.

3.2 Internal wave energy

Contour plots of the energy density averaged over one tidal period indicate the relative strength of the internal wave beam generated by the topography. **Figure 3.2** compares the energy density for cases 1A, 1C (both supercritical) and 1E (transitional). Wave beams originating from the edges of the ridge are clearly visible in each case. In **Figure 3.2a**, the step topography on the east side produces a strong wave beam from the right face of the ridge. The wave beam is nearly vertical between 200 and 400 m because of the weak stratification in the water column. The wave beam then splits into two wave beams at 200m, a stronger one propagating to the east and a weaker one propagating to the west. After reaching the surface, both wave beams are trapped by the strong stratification in the upper ocean. A similar but weaker wave beam also develops on the left face. Two wave beams away from the ridge on each side can therefore be seen in the two upper panels of **Figure 3.2**. Thus the internal wave beams leaving the ridge are contributed to by both sides

of the ridge. However, the wave beams propagating toward the centre of the ridge are out of phase with the outward propagating waves and therefore do not contribute as much energy.

ISWs are characterized by oscillations in the density field, with a sharp leading edge and strong downward flow. On leaving the ridge, a mode one wave forms and develops into an ISW on either side of the topography, indicating that the slopes on both sides of the ridge are supercritical. In experiment 1A (**Figure 3.2a**), the step function on the right side of the ridge generates a large amount of energy. Most of the energy propagates to the east in a wide wave beam. A strong ISW, with a sharp downward leading edge forms at approximately 120 km from the origin. The weaker narrower wave beam to the west of the ridge also forms an ISW. It is weaker than its counterpart to the east, with a shallower leading edge and smaller amplitude.

In the case of a steep finite slope on the right side (**Figure 3.2b**) internal waves are generated on both sides of the ridge, combining over the plateau in the center of the domain. Similar to 1A (**Figure 3.2a**), the wave beam generated on the right side of the ridge divides at $z \approx 200$ m, propagating energy in both directions. The maximum energy value at the surface is larger than **Figure 3.2a** on the west of the domain and smaller on the east,

due to the difference in energy contributed from the right slope. ISWs are still present on both sides. However, the energy in the ISW on the east side is comparable to that on the west side and is less than in **Figure 3.2a** because of the less steep right slope. In the final panel **Figure 3.2c**, the energy density generated on both sides of the ridge has decreased, with a wave beam nearly invisible at the right topography slope. The maximum energy density at the surface is also lower on both sides and the ISW packets that appear are less intense.

Figure 3.3 compares the energy density for cases 1H (transitional), 1K and 1M (subcritical). Comparing **Figure 3.3a** to **Figure 3.2c**, the energy density is much lower than in 1E. Wave beams are generated only on the left side of the ridge and propagate toward both directions. No ISWs form on either side. The decrease in maximum slope on the right side of the topography is observed to have a significant impact on both sides of the model domain. This trend is continued in **Figure 3.3b**. The internal waves still propagate from the left side of the ridge in the subcritical case 1K with slightly smaller peak energy values than that in 1H (8 J/m^3). **Figure 3.3c** shows the weak energy generation associated with case 1M, approximately eight times smaller than case 1C. The continental shelf topography significantly decreases the energy on both sides of the model domain. The internal wave is

broadly symmetrical, with some modification to the wave beam on the east side due to the shelf topography.

The experiments with varying slope on one side of the ridge indicate that wave beams are generated only from supercritical slopes. When both slopes are supercritical, wave beams form on both sides of the ridge and strong internal waves propagate away from the ridge in both directions. If the slope on one side of the ridge is transitional or subcritical, the strength of the internal wave is greatly reduced. Waves are now contributed only from the supercritical side of the ridge but internal waves propagating in both directions are of comparable strength.

3.3 Baroclinic energy flux

The vertically integrated horizontal energy flux is displayed as a function of x in **Figure 3.4** for the four supercritical cases 1A, 1B, 1C and 1D. The transitional and subcritical cases are similarly displayed in **Figure 3.5** and **Figure 3.6** respectively. The flux is averaged over the same tidal period as in **Figures 3.2**. Negative (positive) values indicate a westward (eastward) flux. The steepest increases occur over the ridge slopes, where the internal wave beam is generated (as observed in **Figure 3.2**). The flux then reaches a constant value away from the topography. ISWs are observed as large oscillations in magnitude of energy flux.

The flux across the ridge is close to zero in all four supercritical cases, with a small westward flux in case 1B and 1C due to the right ridge slope being steeper. To the west of the ridge, the flux reaches a maximum value at the horizontal extent of the ridge topography, $x \approx -30$ km. This maximum value is similar for 1B, 1C and 1D, suggesting the westward flux is independent of the eastward slope in this supercritical region. The westward flux is slightly less in the case 1A, implying there is some energy dissipation caused by the step topography on the right of the ridge. ISW packets of similar intensity form at $x \approx -150$ km. To the right of the plateau, the varying slope width changes the lateral extent of the topography. This is observed in the location of the maximum flux, which moves further to the right of the domain as slope width increases from 0 to a finite value. Cases 1B, 1C and 1D are qualitatively similar, with a steep increase over the topographic slope reaching a maximum at $x=24$ km, $x=27$ km and $x=31$ km respectively. The flux then continues at this maximum value before forming an ISW at approximately the same distance to the right of the ridge topography. In the case 1A, the step function causes a jump in the flux at the right ridge edge. Unlike the other supercritical cases, the flux initially decreases away from the ridge, before forming an ISW packet closer to the topography at $x \approx 100$ km. As with **Figure 3.2**, the ISW is stronger to the right of the ridge in 1A than in the other supercritical cases.

For the cases with a transitional slope on the right of the ridge (**Figure 3.5**), the flux over the plateau is positive. Energy from the left side of the topography contributes to the wave beam on the right side. The magnitude of the flux crossing the ridge is inversely related the slope parameter of the right slope, with substantially higher flux contributed in case 1I than in 1E. The westward flux increases to a maximum value at the same location for all transitional cases as 1D ($x = -30\text{km}$), and ISWs are observed for the two cases closest to the supercritical range, 1E and 1F. As in **Figure 3.4**, the eastward flux in the supercritical cases increases to a maximum at the lateral extent of the topography. In the transitional cases however, there is a decrease to a lower flux value after the peak flux. Both the maximum flux value and the extent of the decrease are positively related to the east slope parameter. For example, flux in case 1F peaks at 1230 W/m on the east side of the domain, before decreasing to 1112 W/m at 150 km. The flux in case 1H peaks at 998 W/m, before decreasing to 758 W/m at 150 km. As with the westward flux, ISWs form in cases 1E and 1F whereas the others do not.

Figure 3.6 shows the vertically integrated horizontal energy flux in the subcritical cases. The y-axis is of the same scale as in the previous two figures to emphasize the decrease in wave energy. Like the supercritical cases, there is no observable difference between 1J, 1K and 1M to the west of the ridge, each case reaching a constant maximum flux of approximately -

470 W/m at $x = 30$ km. The flux across the plateau is constant in all subcritical cases. The eastward flux from the west side of the ridge to the east side is higher than in either the transitional or supercritical cases. Furthermore, the cross plateau flux (420 W/m) is approximately the same as the westward flux from the left edge of the topography. On crossing the right slope, the flux increases, with a larger increase in the case of a steeper slope. As with the transitional cases, this flux quickly decreases to a lower value. The steady flux value reached at $x=150$ km is slightly lower than the contribution from the supercritical left side of the ridge, suggesting the subcritical right side dissipates more energy than it contributes. In this respect, 1M does not agree well with the other subcritical cases. The energy flux on both sides of the ridge is much smaller, and remains constant away from the topography. No ISW packets are generated in any of the subcritical cases.

To summarize, topography with two supercritical slopes will not generate significant net energy flux across the ridge, but will generate large internal waves propagating away from the topography, which develop into ISWs. A ridge with one supercritical slope and one subcritical slope will generate energy flux of approximately equal strength in both directions, but the cross plateau wave will weaken as it crosses the subcritical right slope. In the transitional range, the internal wave generated away from the topography by the supercritical slope will decrease in strength as the adjacent slope decreases. The cross

plateau flux from the steeper side increases as the slope parameter on the other side decreases. Dissipation reduces the flux leaving the less steep slope, resulting in a small east-west asymmetry in energy flux. ISW packets are observed in this range only for $\gamma > 1.5$.

3.4 Additional experiments

In addition to the variation in internal wave energy caused by decreasing the slope parameter on one side of the ridge, a number of supplementary experiments have been carried out (**Table 2.2**). Here, three model parameters are examined: the width of the topography plateau, the application of a steady current and the latitude.

3.4.1 Plateau Width

Case 1D is compared with experiment 1a from *Qian et al. (2010)*, referred to as 2A for the purposes of this study. The two model setups differ only in the ridge design; while both experiments have symmetrical slopes of $L = 15\text{km}$, the 1D case has a plateau width of 20 km, unlike 2A which has no plateau (bell shaped ridge).

Figure 3.7 shows the energy density field for the two cases. The internal wave beams in 1D propagate from the edge of the west and east slopes at $x = -15\text{ km}$ and $x = 15\text{ km}$ respectively. In the case of a bell shaped ridge, all internal waves are generated from the origin of the

topography, $x=0$ km in a steep vertical wave beam. The surface maxima of 2A and 1D differ due to this difference in generation site. Averaged over the tidal period, the energy density is more evenly distributed in 1D with lower peak values than in 2A where the wave beam first reflects from the surface. However in 1D the ISW formed on both sides of the ridge is stronger, with a steeper wave front, due to the combination of internal wave energy from both sides of the ridge plateau.

The energy flux of 1D is higher than in 2A on both sides of the domain (**Figure 3.8**), confirming an increase in energy flux due to the leeward propagation of internal wave energy generated on the opposite side of the ridge, not observed in the case of 2A. Although in both cases ISWs form at approximately the same time, the peak energy flux values occur later in the 1D case. No transition zone between east and west is present in 2A, due to the lack of a plateau. In general, topography with a narrow plateau increases the wave energy flux, and the possibility for ISWs formation as four wave beams are generated, whereas only two are generated by a bell shaped ridge. It should be noted that the F' values in *Qian et al. (2010)* were calculated from peak flux rather than the averaging method applied here, so are slightly different.

3.4.2 Steady current

Figure 3.9 compares the energy density field for 1D (**Figure 3.9b**) with and without a steady westward current. **Figure 3.9a** shows case 2B, where a westward steady barotropic mean flow has been applied throughout the water column and **Figure 3.9c** shows case 2C where the current decays exponentially from the sea surface with a decay scale of 50m. The transport in each case is given in Table 2. In **Figure 3.9a**, the wave seems stronger on the ridge top but ISWs formed away from the ridge are weaker. In **Figure 3.9c** the wave beam is wider than in **Figure 3.9b**, with a maximum on the west topographic slope not observed in 1D. The energy at the surface is slightly diminished by the mean flow and the leading edge of the ISW is shallower on the west side of the domain. The most significant differences between 1D and 2C in **Figure 3.9c** are in the surface layer, $z > -100\text{m}$. An increase in the peak energy is shown at each instance the internal wave is reflected downward by the surface. The strength of the ISW increases on both sides of the domain. There is no significant impact to the internal wave energy field beneath $z = -100\text{m}$.

The vertically integrated baroclinic energy flux of the three cases (1D, 2B, 2C) is shown in **Figure 3.10**. Unlike in 1D, where the flux across the ridge plateau is zero, a small eastward flux occurs in 2B and there is flux in both directions in 2C. Away from the ridge topography, there are no significant differences between 1D and 2B. Although the amplitude of the flux is not significantly different from the other two in 2C, the current flow is unstable,

observable in the large scale oscillations in both positive and negative fluxes. In general, for the given transport values, the three experiments have similar energy flux away from the ridge. A mean current such as the SEC will not have a significant impact on the energy flux of internal waves.

3.4.3 Latitude

Most internal wave study sites are located in the tropics and lower latitudes (**Figure 1.2**), with some notable exceptions such as the Barents Sea (*Kurkina and Talipova, 2011*). Here, the model sensitivity to latitude is briefly tested. All of the experiments in **table 2.1** were conducted at latitude 15 °S. **Figure 3.11** compares the vertically integrated energy flux for case 1D with the same experiment at the equator (2D), 20 °S (2E) and 60 °S (2F). There is no significant difference between 1D and 2D. Experiment 2E is quantitatively similar to 1D, but reaches a lower flux value on both sides of the ridge topography. However, the ISWs produced by all three cases are of approximately the same magnitude at $|x| \geq 175$ km. It is only the highest latitude case, 2F, which does not form ISWs. The internal wave flux decays away from the topography to a minimum at the model domain boundary, in a similar fashion to the subcritical range in **Figure 3.3b**. The model is shown to be insensitive to changes in latitude near the equator, with a rapid decrease in energy flux as latitude

increases. 2F is approaching the critical latitude at 75°S, beyond which internal waves will not propagate.

4. Mascarene Plateau

4.1 Model results

Here the 1G case is studied in more detail. This experiment is designed to match the topography of the Mascarene Plateau as closely as possible. The east slope is in the transition range, $\gamma = 1.18$ (**Figure 3.1**). The velocity field in the upper 400m of the water column over the whole tidal cycle gives a picture of the generation mechanism. In **Figure 4.1**, each panel is 3 hours apart, with the first panel showing the maximum tidal flow to the east. A wave beam is generated from the steeper west edge of the topography. The positive u value indicates that the wave is generated in the phase of a positive tidal current. In the second panel, the tidal current reaches zero. Here, no internal wave beam appears. Internal waves from the previous wave beam are now propagating in both directions with a phase speed of 1.52 m/s. As the tidal flow reverses (panel 3), an internal wave beam with negative velocity is generated, again on the west side of the ridge. Moving eastward, the weaker internal wave generated in the first panel is enhanced as it moves over the subcritical topography on the east side of the ridge. In the final panel, the tidal current has again reached zero, and the process repeats. As waves move away from the topography, the leading edge steepens forming a weak front.

Figure 4.2 plots the energy density field in the x-z plane. Energy is generated on both sides of the topography. Beneath the strongly stratified thermocline ($z=200\text{m}$), the wave beam from the west slope of the ridge is stronger. Like the subcritical range, the westward wave is also stronger than its eastward counterpart. The maximum energy value occurs at approximately $x=0\text{ km}$, suggesting that internal wave energy from both sides of the ridge is coalescing at this point, with stronger propagation to the west.

The vertically integrated baroclinic energy flux is shown in the x-t plane (**Figure 4.3**). Here, the internal waves propagate away from the centre of the ridge at a phase speed of 1.52 m/s . As with **Figure 3.4** negative flux (yellow) is westward and positive flux (blue) is eastward. At the Mascarene Plateau, the waves propagating in both directions are generated from the maximum west slope, at $x = -15\text{km}$. This is not observed in the highly critical cases, where internal waves are generated from both sides of the topography separately. Although the east side of the ridge is clearly contributing to the overall internal wave energy, it is not a major source of internal wave energy. The peak flux values are observed as deeper blue areas at approximately $x = 30\text{km}$ in the eastward propagating internal waves. ISWs are formed beyond 200 km on the left side of the ridge. On the right side, only slightly intensified wave fronts are visible. This is farther from the ridge than in the supercritical cases, indicating that internal wave amplitude is smaller. The picture that

forms then is of an internal wave generated on the west side of the topography, with stronger energy flux in the west direction. The east internal wave is reinforced by energy from the east side of the topography, with some energy dissipating over the subcritical east ridge slope. ISWs form at a distance greater than 200 km from the centre of the plateau.

4.2 Mode 2 waves

Both *Konyaev et al.* (1995) and *da Silva et al.* (2011) commented on the existence of mode 2 waves at the Mascarene Plateau, citing both SAR images and thermocline displacement records. The model does not reproduce these mode 2 waves in experiment 1G, but they are observable in the most supercritical case. A contour plot of the vertically integrated baroclinic energy flux on the $x-t$ plane in experiment 1A is shown in **Figure 4.4**. Mode 2 waves are generated on the east side of model domain and propagate eastward between $x=0$ and $x=100\text{km}$. The phase speed of 0.4ms^{-1} is slower than the mode 1 waves and is consistent with *da Silva et al.* (2011). The mode 2 waves are not observed in any of the other experiments performed in this study, suggesting that they are only generated by the model when both slopes of the ridge are supercritical.

5. Discussion

Internal waves form as a barotropic tide moves over a steep ridge, propagating away from the topography as a wave beam. If the internal wave amplitude is large enough, it will develop into an ISW. For a given tide, the energy required to form internal waves is dependent on the ridge slope exceeding a critical threshold; regions of critical slope act as sources of energy flux in the lower modes (*Garrett and Kunze 2007*). In this study, the same tidal flow produced internal waves of varying energy, depending on the critical value of the slope parameter on one side of the ridge, where the other slope remained constantly supercritical ($\gamma=2.6$).

In the supercritical range, wave beams propagate vertically from both ridge slopes, becoming horizontal as the water column becomes less stratified. The wave beam splits into eastward and westward components, one moving away from the topography and the other toward the center of the domain. The two wave beams moving in the same direction are not in phase, due to the plateau width between the two slopes. A ridge with a flat plateau generates more energy flux than a bell shaped ridge of the same slope parameter, indicating that the internal waves moving over the topography from the ridge slope have an amplifying effect on the internal waves moving outwards. The energy flux does not increase significantly with increasing slope parameter in this range.

In the transitional range a vertical wave beam is generated only on the supercritical ridge slope. The energy flux at the other slope is mainly over the flank of the ridge, rather than as a concentrated wave beam (Figure 4b *Qian et al.* 2010). The normalized energy flux F' decreases monotonically with slope parameter on both sides of the model domain, as less energy is contributed to the wave beam developed on the supercritical side of the ridge. A similar result was obtained by *Khaliwala* (2003) for a bell shaped ridge of fixed height with varying wave slope α . Energy crosses from the supercritical side to the subcritical side. As the right slope parameter decreases, the left supercritical slope contributes more flux to the wave propagating to the right. In the subcritical range, the energy flux in both directions reaches a minimum, whereas a large flux crosses the ridge. Energy is now dissipated over the subcritical slope, and the flux in each direction is approximately four times less than in the supercritical range.

For the tidal velocity in this study, ISWs do not form on internal waves generated by a ridge with one subcritical slope. ISW formation only occurs in the higher transitional cases and supercritical cases ($\gamma > 1$). ISWs develop farther from the topography in the transitional range than in the supercritical range, and in no case do they develop < 100 km from the centre of the domain. With the exception of the singular cases 1A and 1M, all experiments in this study generated an internal wave of higher intensity on the side of the ridge with

greater slope parameter. Regardless of the difference between the slope parameters on each side of the ridge, the difference in vertically integrated energy flux was approximately 100 W/m. This suggests that this energy dissipated as the internal wave crossed the plateau to the right hand side of the ridge.

In the case of the Mascarene Plateau, the topography in the region is established to be a crucial factor in the asymmetry of internal wave observations. The results of the case study are qualitatively similar to those reported by *da Silva et al.* (2011) with a stronger ISW forming to the west of the ridge. As in observations, the internal waves are generated by the lee wave mechanism on the west side of the ridge. The phase speed and wavelength of the internal waves is larger in the observations than in the model, as the tidal velocity was reduced here for model stability, and to allow comparisons with *Qian et al.* (2010).

Increasing the surface current velocities to match the conditions at the Mascarene Plateau destabilizes the simulation. Strong interactions with the bottom topography created large energy fluxes near the ridge topography. This made it difficult to estimate the internal wave energy flux, and the results are not included here.

The higher tidal velocity in the *da Silva et al.* (2011) study would also account for the lack of mode 2 waves in this study. Mode 2 waves are only observed here in the highly supercritical

case 1A, where the flow becomes supercritical for mode 2 waves (*Stastna and Peltier 2005*). The idealized 2-D topography of the ridge was based on the results of *New et al. (2007)*. This study did not attempt to model realistic topography in the Mascarene Plateau region, using instead an idealized version based on the calculated slope angle and plateau width of the ridge. Imprecise knowledge of ocean bottom topography is a major source of error for this study, and for the accurate modelling of internal waves everywhere (*Llewellyn Smith and Young 2003*), particularly given the high sensitivity of internal wave energy flux to slope steepness.

In this study, the steady westward current at the Mascarene Plateau was simulated in two ways and was not found to have a significant impact on internal wave flux. Applying an exponentially decaying surface current did however show an observable increase in the internal wave energy at the surface. Similarly, *Chavanne et al. (2010)* found an increase in internal wave energy at the surface in the presence of a mesoscale current in the Kauai channel using 3D wave tracing. The question of how much impact ocean currents have on internal waves remains an open one, for which further study is required.

6. Conclusion

A series of experiments are carried out using a three-dimensional nonhydrostatic numerical model to examine the impact of asymmetrical topography on internal wave energy. Internal waves are shown to be less energetic on both sides of the domain as the slope on one side becomes smaller, despite a supercritical slope on one side of the ridge. Although the overall energy generated by the topography decreases markedly with decreasing slope parameter, the difference in flux between the eastward and westward propagating waves remains small in the transitional to subcritical range $\gamma < 2$, with energy on the most critical ridge slope being slightly higher. Energy dissipation as the internal wave crosses the ridge is concluded to be the cause of this discrepancy. In the subcritical range, the energy flux across the topography is higher, as less wave energy is generated from the other slope. Topography with a flat plateau is also shown to generate larger internal waves than a bell shape ridge of the same supercritical slope value, due to the generation and interaction of multiple wave beams.

The Mascarene Plateau is presented as an example of a shallow ridge of asymmetrical topography, which produces higher intensity ISWs to the west than to the east (*da Silva et al. 2011*). Good agreement is shown between the results of this study and the asymmetry of

internal waves in the region, for an idealized two-dimensional ridge. Applying a steady current, designed to simulate the westward SEC in the region, however showed no significant difference to the vertically integrated internal wave flux but a noticeable increase in the energy at the surface if the current is surface intensified as is the case of the Mascarene Ridge. Previous studies (*da Silva et al. 2011, Konyaev et al. 1995*) have suggested this as the cause for the asymmetry of internal waves in the region. This study presents a combination of the topographic asymmetry and the SEC as the primary cause.

This result has implications for internal wave generation over complex topography, particularly if one of the slopes is not supercritical, or if there is a narrow plateau. It cannot be assumed that a single supercritical slope will act as an independent generation site for internal waves in the same way as a bell shaped curve; numerical studies should attempt to model ridges reasonably accurately to predict the full interaction of internal waves with bottom topography.

REFERENCES

- Apel, J. R., H. M. Byrne, J. R. Proni, and R. L. Charnell (1975), Observations of oceanic internal and surface-waves from earth resources technology satellite, *Journal of Geophysical Research*, 80(6), doi: 10.1029/JC080i006p00865.
- Balmforth, N. J., G. R. Ierley, and W. R. Young (2002), Tidal conversion by subcritical topography, *J. Phys. Oceanogr.*, 32(10) doi: 10.1175/1520-0485(2002)032
- Bell, T. H. (1975), Lee Waves in stratified flows with simple harmonic time-dependence, *J. Fluid Mech.*, 67, doi: 10.1017/S0022112075000560.
- Brandt, P., A. Rubino, W. Alpers, and J. Backhaus (1997), Internal waves in the strait of messina studied by a numerical model and synthetic aperture radar images from the ERS 1/2 satellites, *J. Phys. Oceanogr.*, 27(5), 648-663, doi: 10.1175/1520-0485
- Buijsman, M. C., J. C. McWilliams, and C. R. Jackson (2010), East-west asymmetry in nonlinear internal waves from Luzon Strait, *Journal of Geophysical Research-Oceans*, 115, C10057, doi: 10.1029/2009JC006004.
- Cacchione, D. and L. Pratson (2004), Internal tides and the continental slope, *Am. Sci.*, 92(2), 130-137, doi: 10.1511/2004.46.924.
- Chavanne, C., P. Flament, D. Luther, and K. - Gurgel (2010), The surface expression of semidiurnal internal tides near a strong source at hawaii. Part II: Interactions with mesoscale currents, *J. Phys. Oceanogr.*, 40(6), 1180-1200, doi: 10.1175/2010JPO4223.1.
- Chao, S., D. Ko, R. Lien, and P. Shaw (2007), Assessing the west ridge of luzon strait as an internal wave mediator, *J. Oceanogr.*, 63(6), 897-911, doi: 10.1029/2003G1A19077.
- da Silva, J. C. B., A. L. New, and J. M. Magalhaes (2011), On the structure and propagation of internal solitary waves generated at the Mascarene Plateau in the Indian Ocean, *Deep-Sea Research Part I*, 58(3), 229-240, doi: 10.1016/j.dsr.2010.12.003.
- Dossmann, Y., A. Paci, F. Auclair, and J. W. Floor (2011), Simultaneous velocity and density measurements for an energy-based approach to internal waves generated over a ridge, *Exp. Fluids*, 51(4), doi: 10.1007/s00348-011-1121-3.

Garrett, C. and E. Kunze (2007), Internal tide generation in the deep ocean, *Annu. Rev. Fluid Mech.*, 39, doi: 10.1146/annurev.fluid.39.050905.110227.

Hibiya, T. (1986), Generation mechanism of internal waves by tidal flow over a sill, *Journal of Geophysical Research-Oceans*, 91(C6), 7697-7708, doi: 10.1029/JC091iC06p07697.

Jackson C. R. (2004), *An Atlas of Internal Solitary-like Internal Waves*, Global Ocean Assoc., Alexandria, Va.

Kaartvedt, S., T. A. Klevjer, and D. L. Aksnes (2012), Internal wave-mediated shading causes frequent vertical migrations in fishes, *Mar. Ecol. -Prog. Ser.*, 452, 1-10, doi: 10.3354/meps09688.

Khatiwala, S. (2003), Generation of internal tides in an ocean of finite depth: analytical and numerical calculations, *Deep-Sea Research Part I*, 50(1), doi: 10.1016/S0967-0637(02)00132-2.

Klemas, V. (2012), Remote sensing of ocean internal waves: an overview, *J. Coast. Res.*, 28(3), 540-546, doi: 10.2112/JCOASTRES-D-11-00156.1.

Konyaev, K., K. Sabinin, and A. Serebryany (1995), Large-amplitude internal waves at the Mascarene Ridge in the Indian ocean, *Deep-Sea Res. Part I*, 42(11-12), 2075, doi: 10.1016/0967-0637(95)00067-4.

Kurkina, O. E. and T. G. Talipova (2011), Huge internal waves in the vicinity of the Spitsbergen Island (Barents Sea), *Natural Hazards and Earth System Sciences*, 11(3), doi: 10.5194/nhess-11-981-2011.

St. Laurent, L., S. Stringer, C. Garrett, and D. Perrault-Joncas (2003), The generation of internal tides at abrupt topography, *Deep-Sea Research Part I*, 50(8), doi: 10.1016/S0967-0637(03)00096-7.

Lee, C. and Beardsley, R.C. (1974), Generation of long nonlinear internal waves in a weakly stratified shear-flow, *Journal of Geophysical Research*, 79(3), 453-462, doi: 10.1029/JC079i003p00453.

Lien, R. C., T. Y. Tang, M. H. Chang, and E. A. D'Asaro (2005), Energy of nonlinear internal waves in the South China Sea, *Geophys. Res. Lett.*, 32(5), 1A5615, doi: 10.1029/2004G1A22012.

Maxworthy T. (1979) A note on the internal solitary waves produced by tidal flow over a three dimensional ridge, *J. Geophys. Res.*, 84,338-346, doi: 10.1029/JC084Ic01P00338

Moore, S. E. and R. Lien (2007), Pilot whales follow internal solitary waves in the South China Sea, *Mar. Mamm. Sci.*, 23(1), 193-196, doi: 10.1111/j.1748-7692.2006.00086.x.

Morozov, E. G. and V. I. Vlasenko (1996), Extreme tidal internal waves near the Mascarene ridge, *J. Mar. Syst.*, 9(3-4), doi: 10.1016/S0924-7963(95)00042-9.

Morozov, E. G., L. V. Nechvolodov, and K. D. Sabinin (2009), Beam propagation of tidal internal waves over a submarine slope of the Mascarene Ridge, *Oceanology*, 49(6), 745-752, doi: 10.1134/S0001437009060010.

Moum, J., D. Farmer, W. Smyth, L. Armi, and S. Vagle (2003), Structure and generation of turbulence at interfaces strained by internal solitary waves propagating shoreward over the continental shelf, *J. Phys. Oceanogr.*, 33(10), 2093-2112, doi: 10.1175/1520-0485(2003)

Nash, J.D., Moum, J. (2005) River plumes as a source of large-amplitude internal waves in the coastal ocean. *Nature*437, 400-403. doi: 10.1038/nature03936

New, A. L., S. G. Alderson, D. A. Smeed, and K. L. Stansfield (2007), On the circulation of water masses across the Mascarene Plateau in the South Indian Ocean, *Deep-Sea Research Part I*, 54(1), 42-74, doi: 10.1016/j.dsr.2006.08.016.

Peacock, T., P. Echeverri, and N. J. Balmforth (2008), An experimental investigation of internal tide generation by two-dimensional topography, *J. Phys. Oceanogr.*, 38(1), doi: 10.1175/2007JPO3738.1.

Petrelis, F., S. L. Smith, and W. R. Young (2006), Tidal conversion at a submarine ridge, *J. Phys. Oceanogr.*, 36(6), doi: 10.1175/JPO2879.1.

Pomar, L., M. Morsilli, P. Hallock, and B. Badenas (2012), Internal waves, an under-explored source of turbulence events in the sedimentary record, *Earth-Sci. Rev.*, 111(1-2), 56-81, doi: 10.1016/j.earscirev.2011.12.005.

Qian, H., P. Shaw, and D. S. Ko (2010), Generation of internal waves by barotropic tidal flow over a steep ridge, *Deep-Sea Research Part I*, 57(12), 1521-1531, doi: 10.1016/j.dsr.2010.09.001.

- Quaresma, L. S., J. Vitorino, A. Oliveira, and J. da Silva (2007), Evidence of sediment resuspension by nonlinear internal waves on the western Portuguese mid-shelf, *Mar. Geol.*, 246(2–4), 123–143, doi: 10.1016/j.margeo.2007.04.019.
- Ramp, S. R., T. Y. Tang, T. F. Duda, J. F. Lynch, A. K. Liu, C. S. Chiu, F. L. Bahr, H. R. Kim, and Y. J. Yang (2004), Internal solitons in the northeastern South China Sea - Part I: Sources and deep water propagation, *IEEE J. Ocean. Eng.*, 29(4), doi: 10.1109/JOE.840839.
- Ramp, S. R., Y. J. Yang, and F. L. Bahr (2010), Characterizing the nonlinear internal wave climate in the northeastern South China Sea, *Nonlinear Processes in Geophysics*, 17(5), doi: 10.5194/npg-17-481-2010.
- Reeder, D. B., B. B. Ma, and Y. J. Yang (2011), Very large subaqueous sand dunes on the upper continental slope in the South China Sea generated by episodic, shoaling deep-water internal solitary waves, *Mar. Geol.*, 279(1–4), 12–18, doi: 10.1016/j.margeo.2010.10.009.
- Scotti, A., R. C. Beardsley, and B. Butman (2007), Generation and propagation of nonlinear internal waves in Massachusetts Bay, *Journal of Geophysical Research-Oceans*, 112(C10), C10001, doi: 10.1029/2007JC004313.
- Shaw, P. and S. Chao (2006), A nonhydrostatic primitive-equation model for studying small-scale processes: An object-oriented approach, *Cont. Shelf Res.*, 26(12–13), 1416–1432, doi: 10.1016/j.csr.2006.01.018.
- Shaw, P., D. S. Ko, and S. Chao (2009), Internal solitary waves induced by flow over a ridge: With applications to the northern South China Sea, *Journal of Geophysical Research-Oceans*, 114, C02019, doi: 10.1029/2008JC005007.
- Shroyer, E. L., J. N. Moum, and J. D. Nash (2010), Vertical heat flux and lateral mass transport in nonlinear internal waves, *Geophys. Res. Lett.*, 37, 1A8601, doi: 10.1029/2010G1A42715.
- Smith, S. G. L. and W. R. Young (2003), Tidal conversion at a very steep ridge, *J. Fluid Mech.*, 495, doi: 10.1017/S0022112003006098.
- Stastna, M. and W. R. Peltier (2005), On the resonant generation of large-amplitude internal solitary and solitary-like waves, *J. Fluid Mech.*, 543, doi: 10.1017/S002211200500652X.

Vlasenko, V. I. and E. G. Morozov (1993), Generation of Semidiurnal Internal Waves Over a Submarine Ridge, *Okeanologiya*, 33(3).

Vlasenko, V. and K. Hutter (2002), Numerical experiments on the breaking of solitary internal waves over a slope-shelf topography, *J. Phys. Oceanogr.*, 32(6), 1779-1793, doi: 10.1175/1520-0485

Zheng, Q., R. D. Susanto, C. Ho, Y. T. Song, and Q. Xu (2007), Statistical and dynamical analyses of generation mechanisms of solitary internal waves in the northern South China Sea, *Journal of Geophysical Research-Oceans*, 112(C3), C03021, doi: 10.1029/2006JC003551.

Table 2.1: List of experiments.

Experiment name	Variable slope width (L in km)	Slope parameter (γ)
1A	0	→ Inf
1B	10	3.54
1C	12	2.95
1D	15	2.36
1E	18	1.97
1F	23	1.57
1G	30	1.18
1H	38	0.93
1I	45	0.79
1J	60	0.59
1K	78	0.45
1L	130	0.27
1M	infinity	0.00

Table 2.2: List of secondary parameter experiments.

Experiment name	Base experiment	Variation from base experiment
2A	1D	Plateau width = 0 km, 20km in original case
2B	1D	Additional 2.5 cm/s barotropic mean flow
2C	1D	Additional 10 cm/s current decaying exponentially with depth
2D	1D	Latitude = 0°, 12.5° in original case
2E	1D	Latitude = 20°
2F	1D	Latitude = 60°

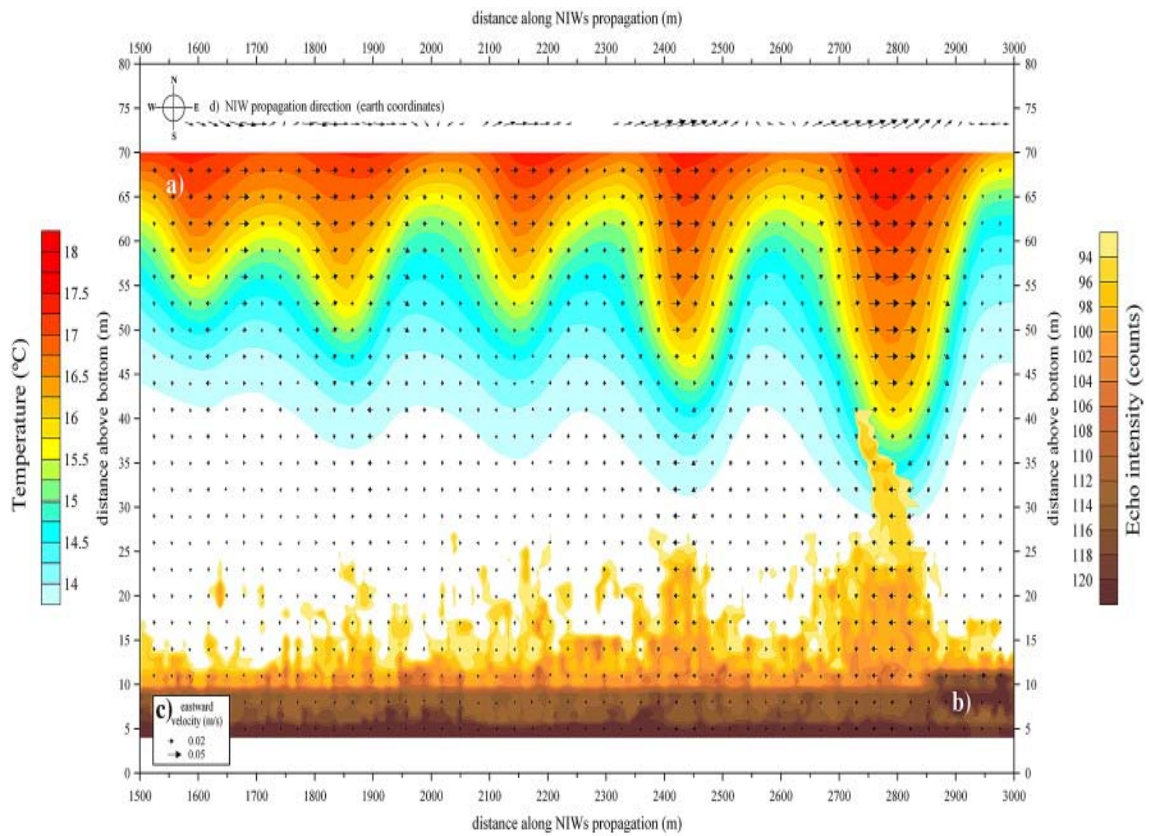


Figure 1.1. Internal wave propagation in the temperature field. Wave propagates from left to right at the western Portuguese mid-shelf, with the leading edge on the far right (adapted from *Quaresma et al. 2007*)

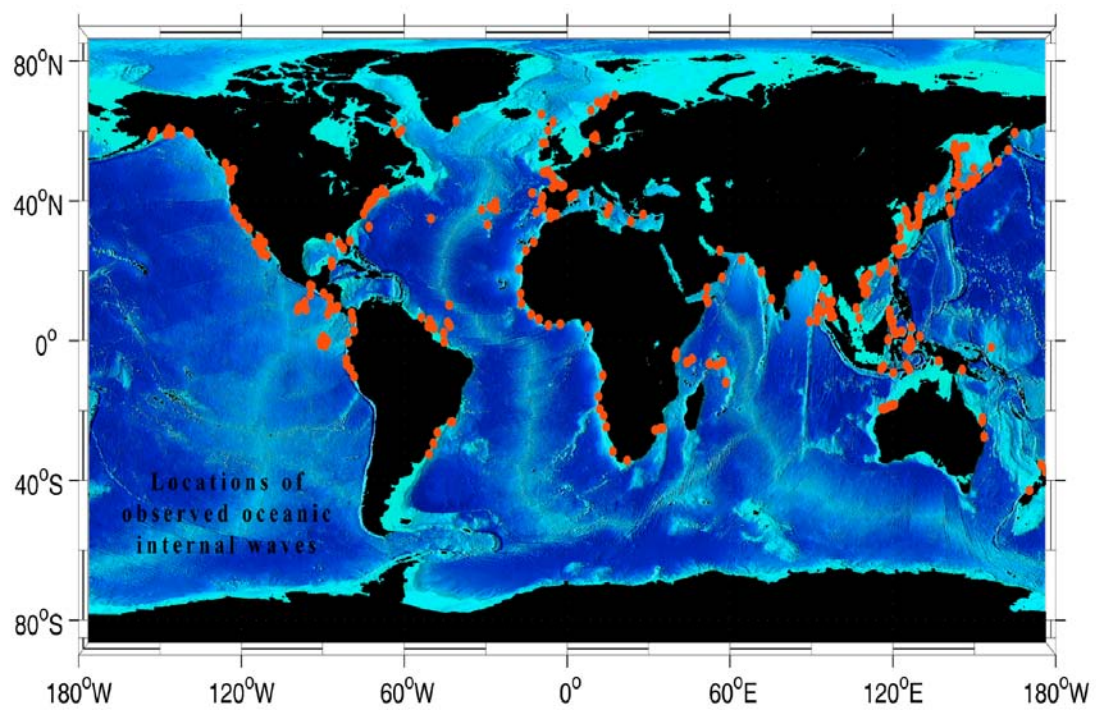


Figure 1.2. Map of recognized internal wave locations (adapted from *Jackson, 2004*)



Figure 1.3. Satellite image of surface modulations caused by internal waves at the Straits of Gibraltar from <http://envisat.esa.int/handbooks/asar/CNTR1-1-5.html>

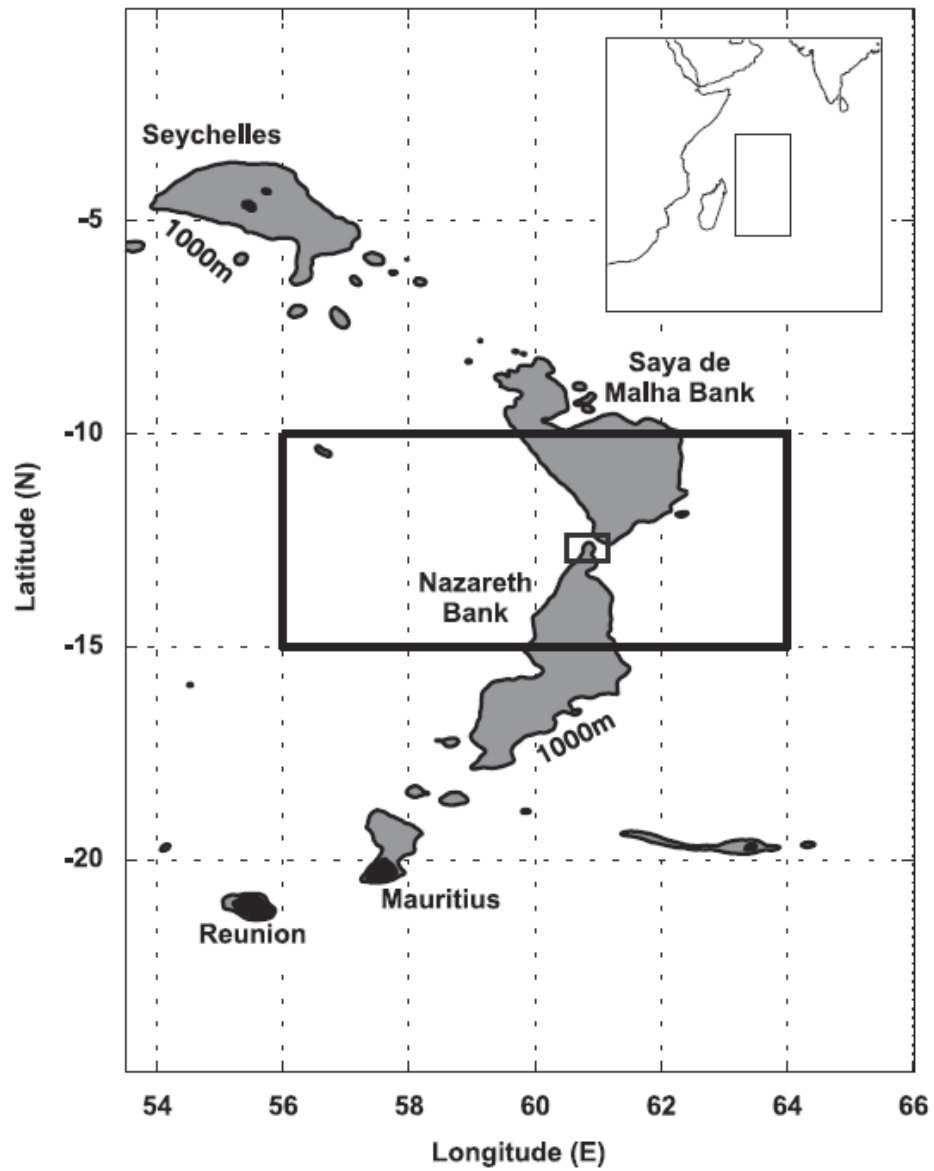


Figure 1.4. Map of the Mascarene Plateau from *da Silva et al.* (2011). The source region of the internal waves between the two shallow water banks is highlighted. Grey regions represent areas shallower than 1000m and dark regions represent land

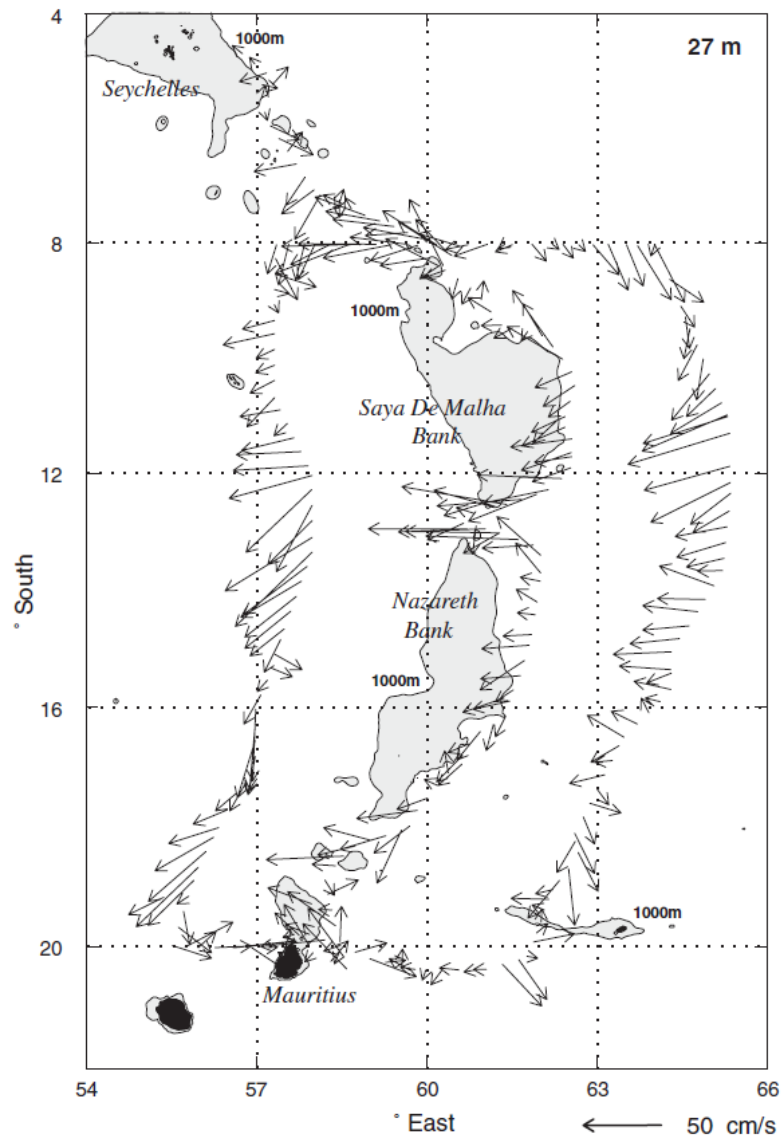


Figure 1.5. Surface currents at the Mascarene Plateau, adapted from *New et al.* (2007)

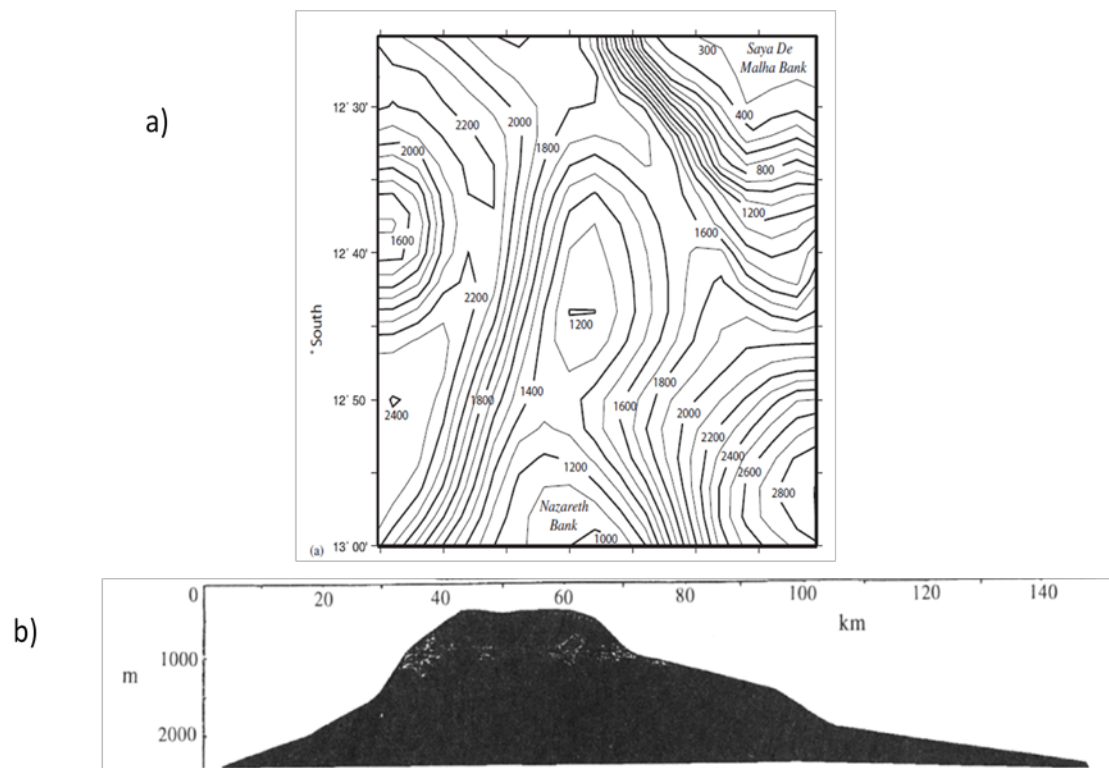


Figure 1.6. Topography of the Mascarene Plateau, a) in plan view (*new et al.* 2007) and b) in profile (*Konyaev* 1995). The depth contours in a) are in meters

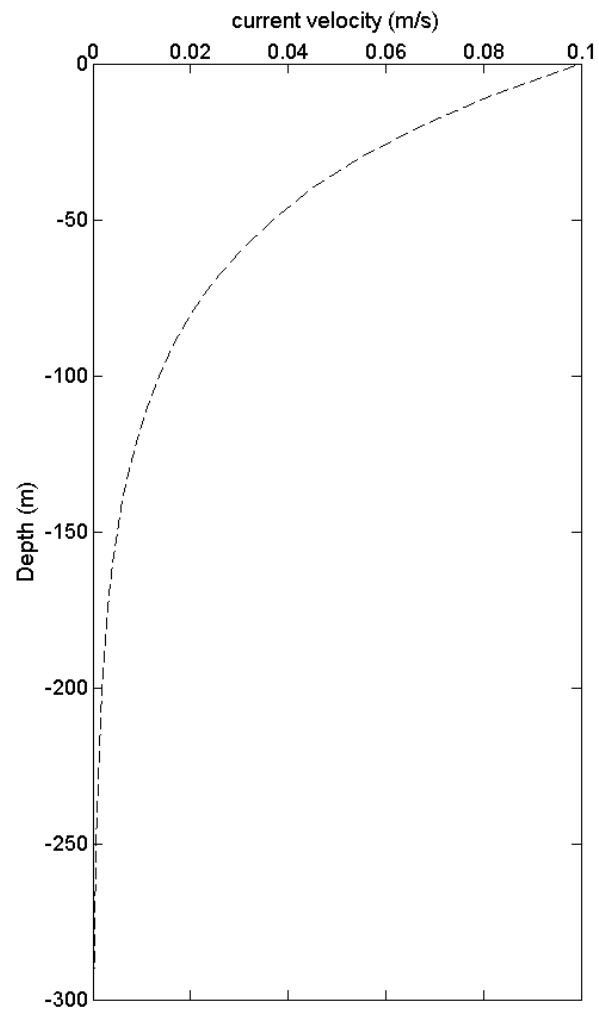


Figure 2.1. Current profile used in the numerical study. The value of U_m is 10 cm s^{-1} at the surface and decreases exponentially with depth

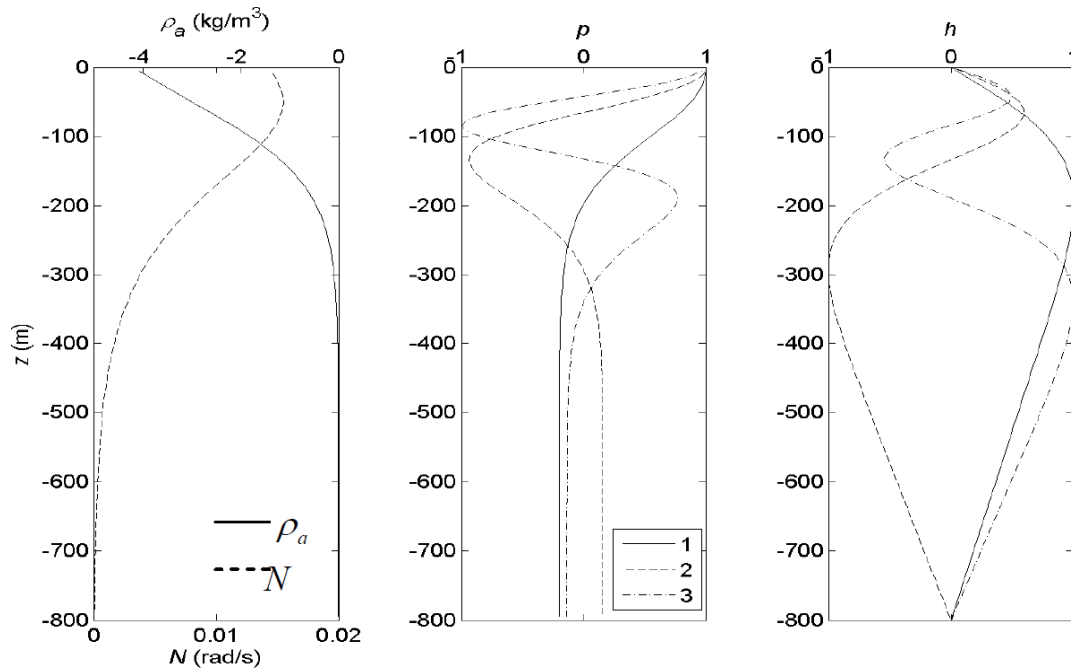


Figure 2.2. (a) Density ρ_a in kg m^{-3} and buoyancy frequency N in rad s^{-1} in all experiments listed in tables 2.1 and 2.2. The corresponding normal modes are shown (b) for horizontal velocity and (c) for density perturbation. The phase speeds are 1.52, 0.64, and 0.41 m s^{-1} for the first three modes. From *Shaw et al.* (2009)

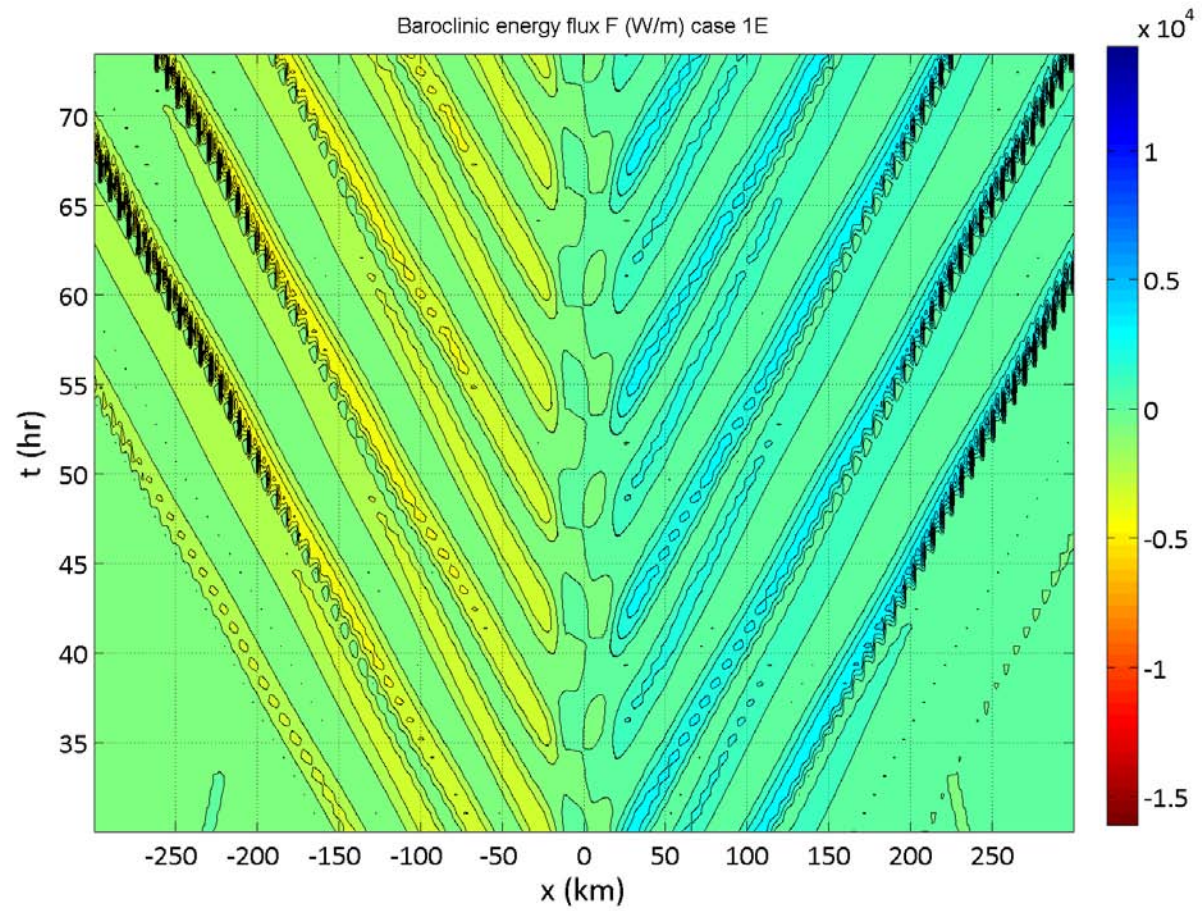


Figure 2.3. Study area A, enclosed in a dotted line on a baroclinic energy flux plot in the x - t plane. The Contour interval is 1000 (W/m)

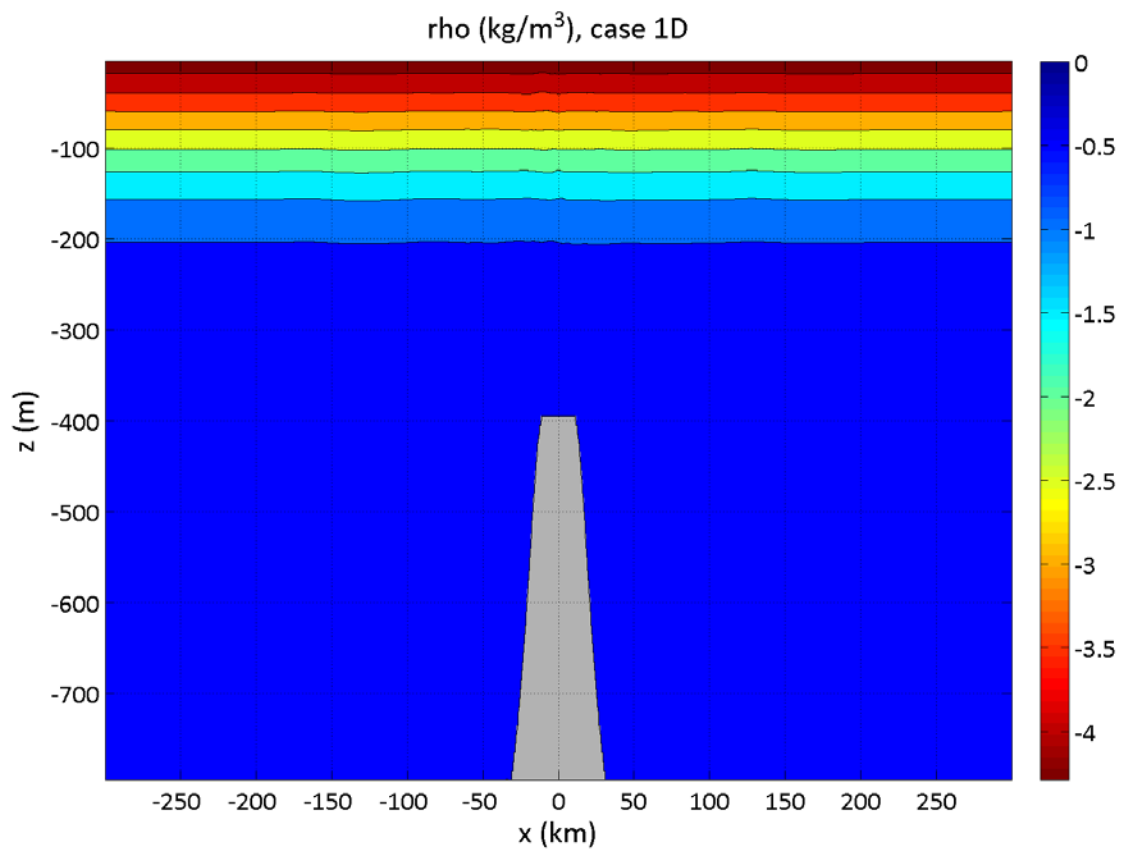


Figure 2.4. The model configuration. Contours show the background density field averaged over 12 hours for case 1D. The model is forced by a semidiurnal tide

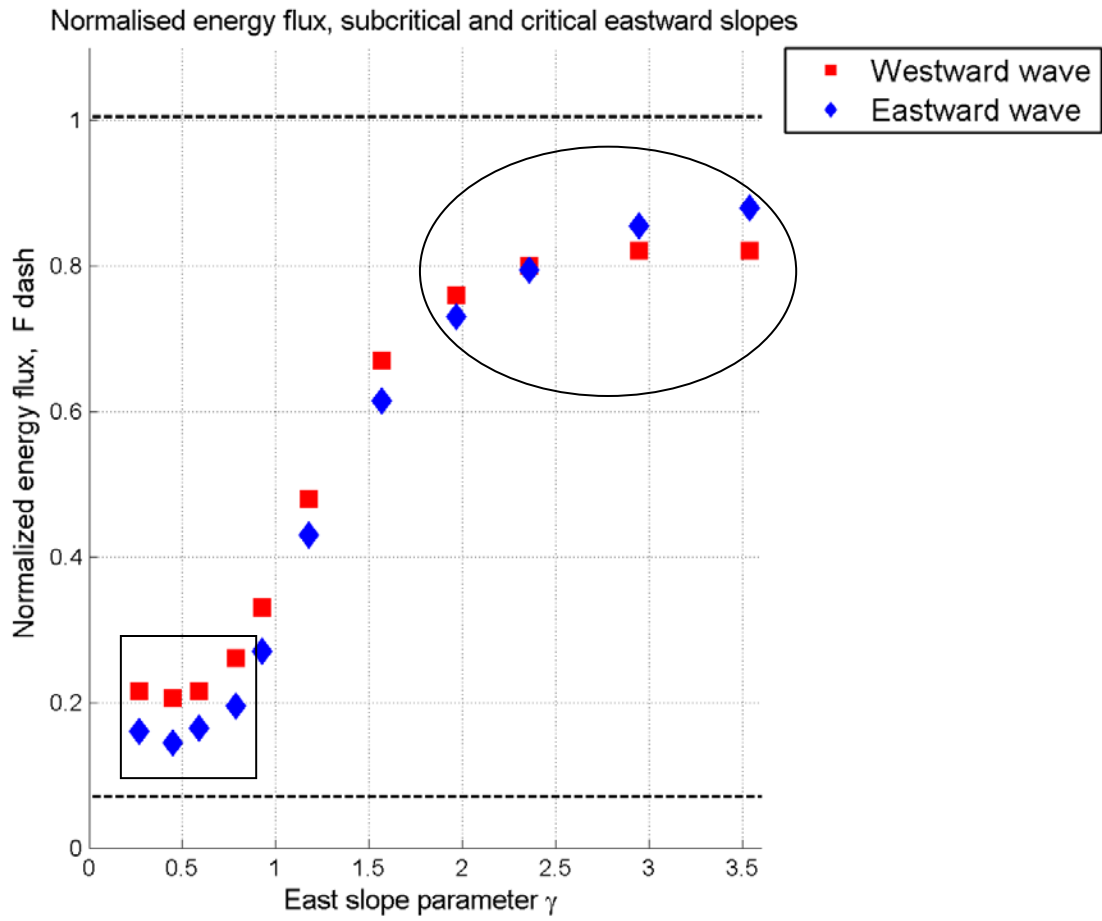


Figure 3.1. Normalized energy flux as a function of slope parameter, for all cases. The subcritical and critical ranges of γ are enclosed by a rectangle and an oval respectively. The energy levels for the end members of the experiment series (1A and 1M) are plotted as black dotted lines

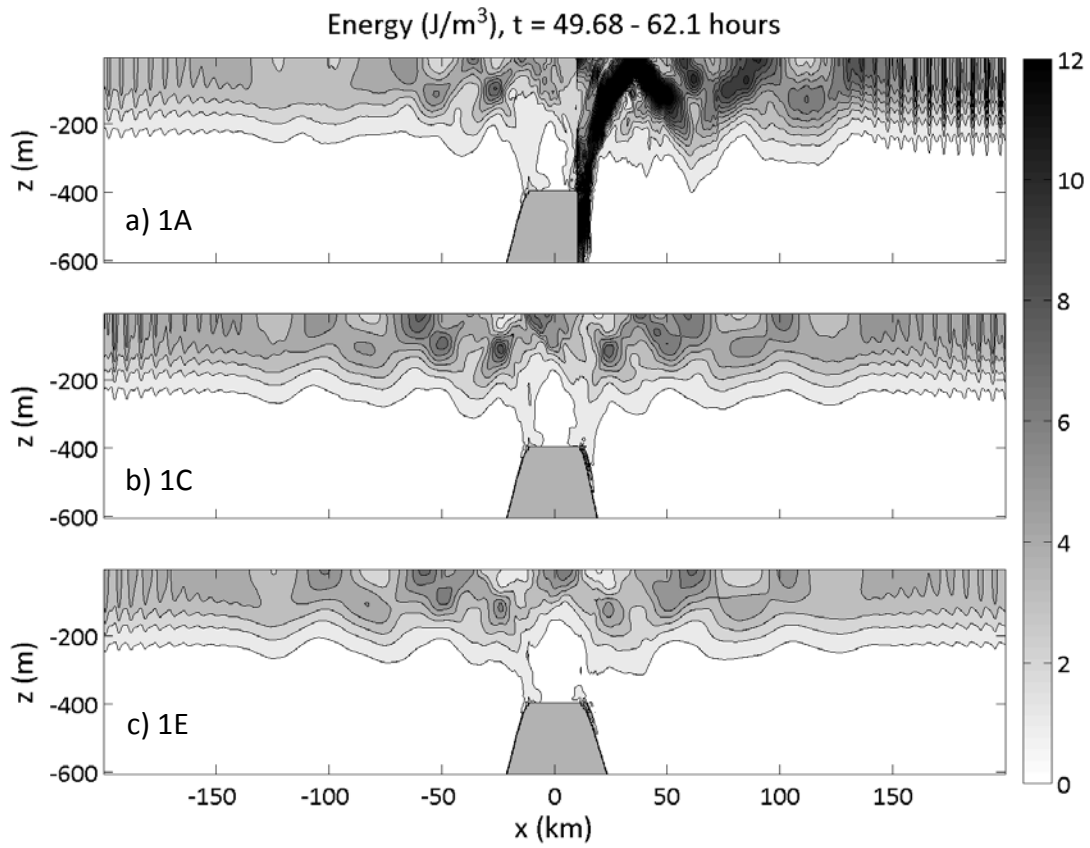


Figure 3.2 Internal wave energy density (J/m^3) averaged over one tidal cycle 49.70 – 62.10 hours, for L equal to (a) 0 km (b) 12 km and (c) 18 km. The width of the slope on the left is 15 km. The contour interval in all panels is 1 J/m^3

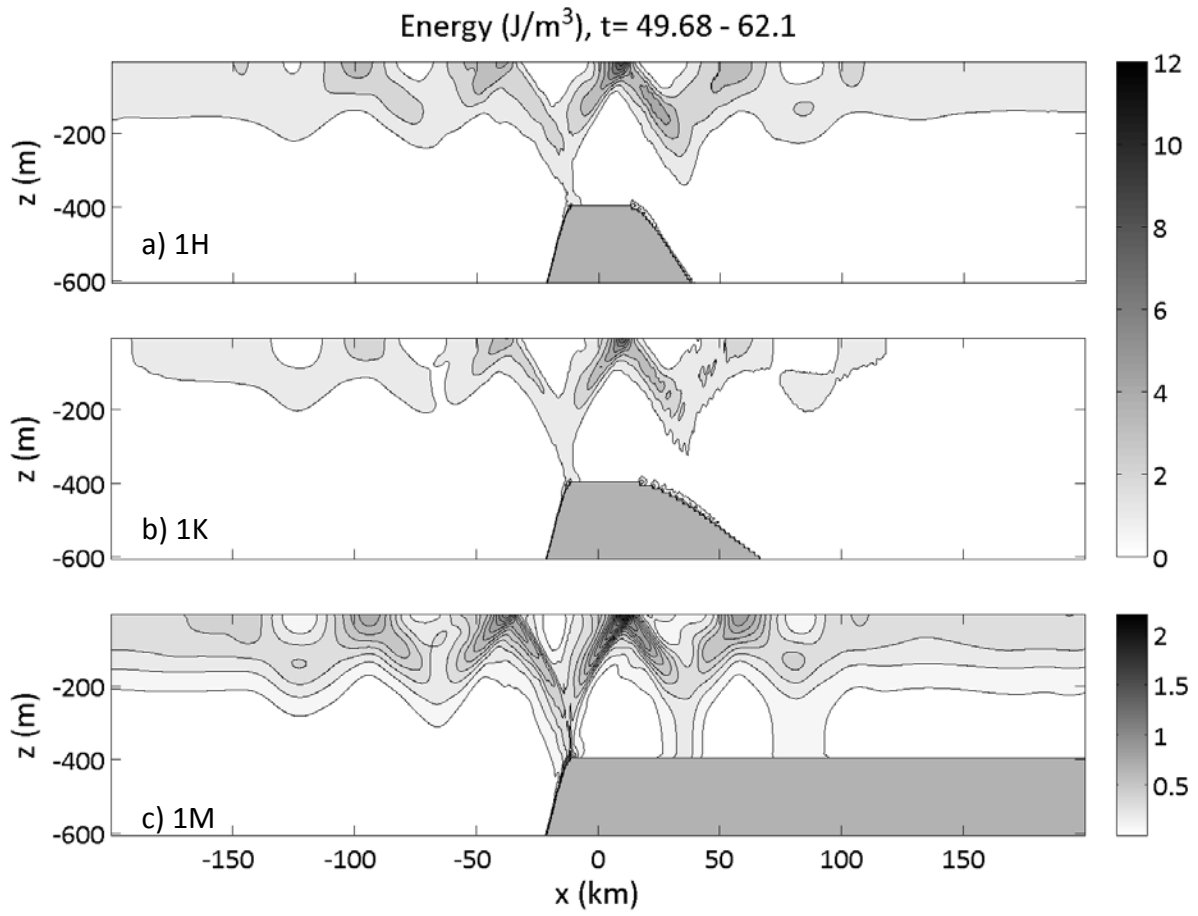


Figure 3.3. Same as Figure 3.2 but for L equal to (a) 38 km (b) 78 km and (c) infinity. The contour interval in the top two panels is 1 J/m^3 and 0.1 J/m^3 in the bottom panel

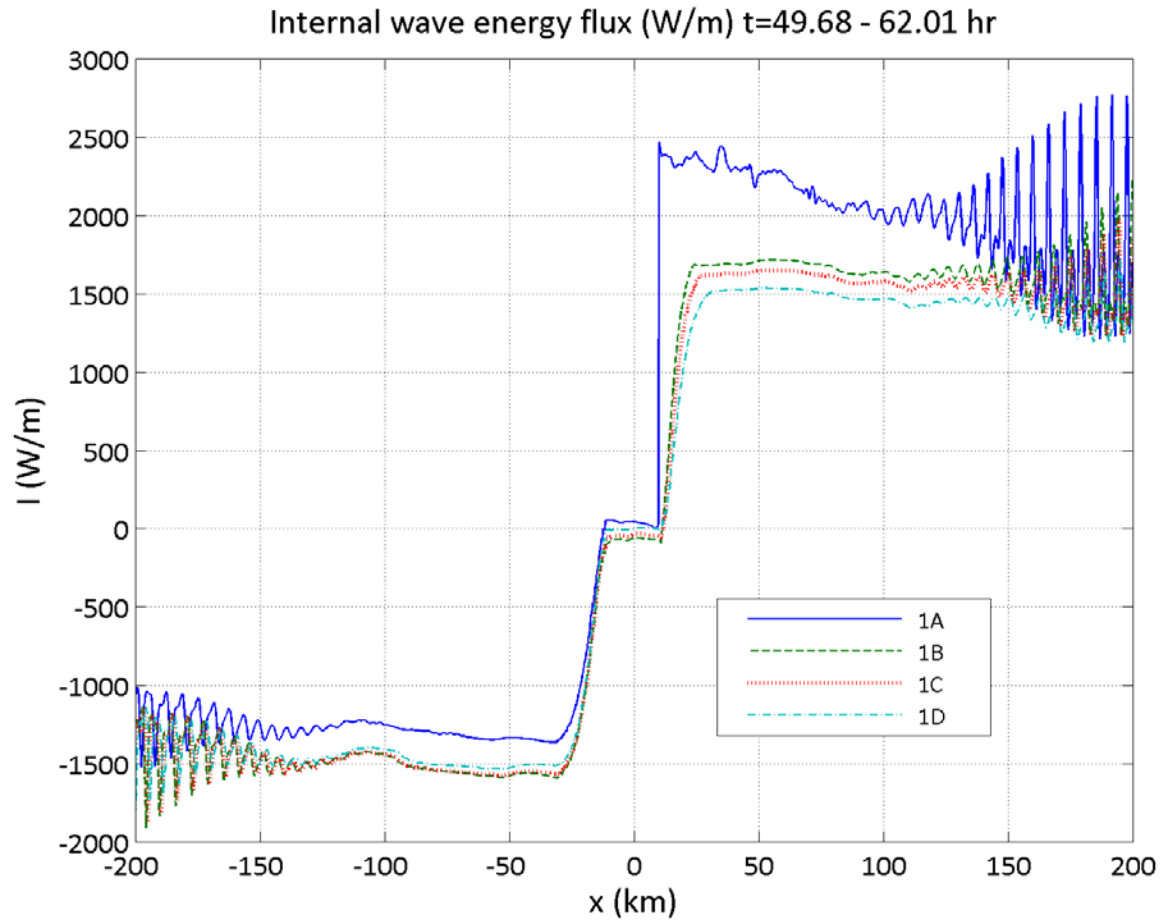


Figure 3.4. Vertically integrated horizontal energy flux (W/m) as a function of x for the supercritical experiments 1A, 1B, 1C and 1D. The flux is averaged over the tidal cycle 49.68 – 62.10 hours. The ridge is located at $x=0$ km.

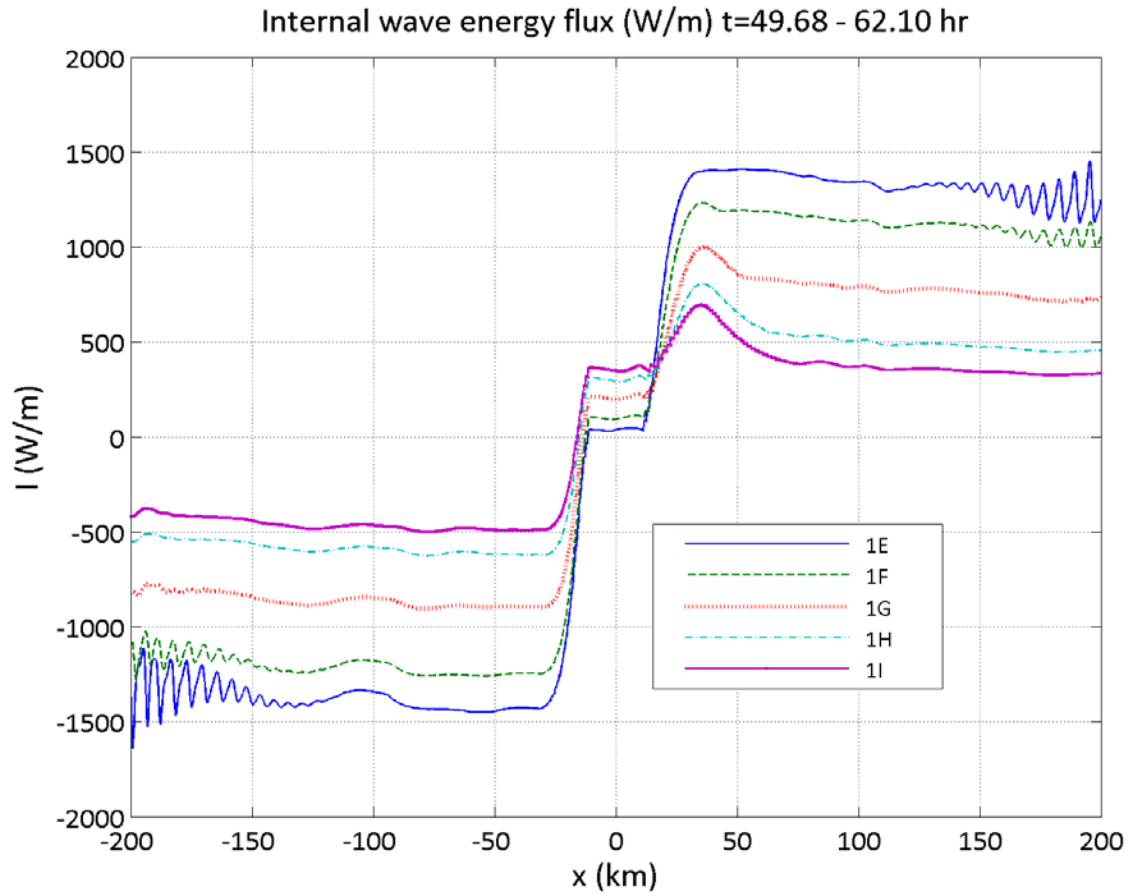


Figure 3.5. Vertically integrated horizontal energy flux (W/m) as a function of x for the transitional experiments 1E, 1F, 1G, 1H and 1I. The flux is averaged over the tidal cycle 49.68 – 62.10 hours. The ridge is located at $x=0$ km

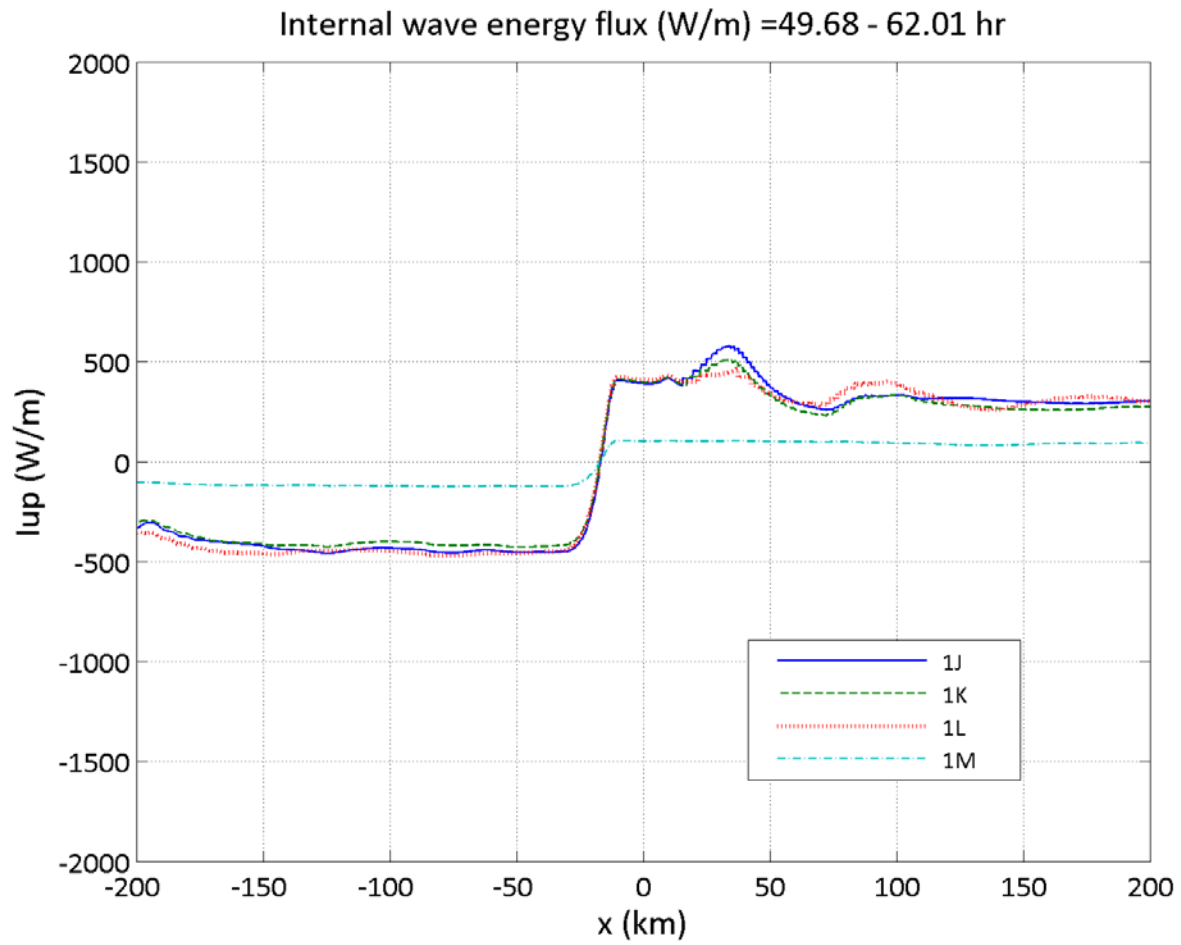


Figure 3.6. Vertically integrated horizontal energy flux (W/m) as a function of x for the transitional experiments 1E, 1F, 1G, 1H and 1I. The flux is averaged over the tidal cycle 49.68 – 62.10 hours. The ridge is located at $x=0$ km

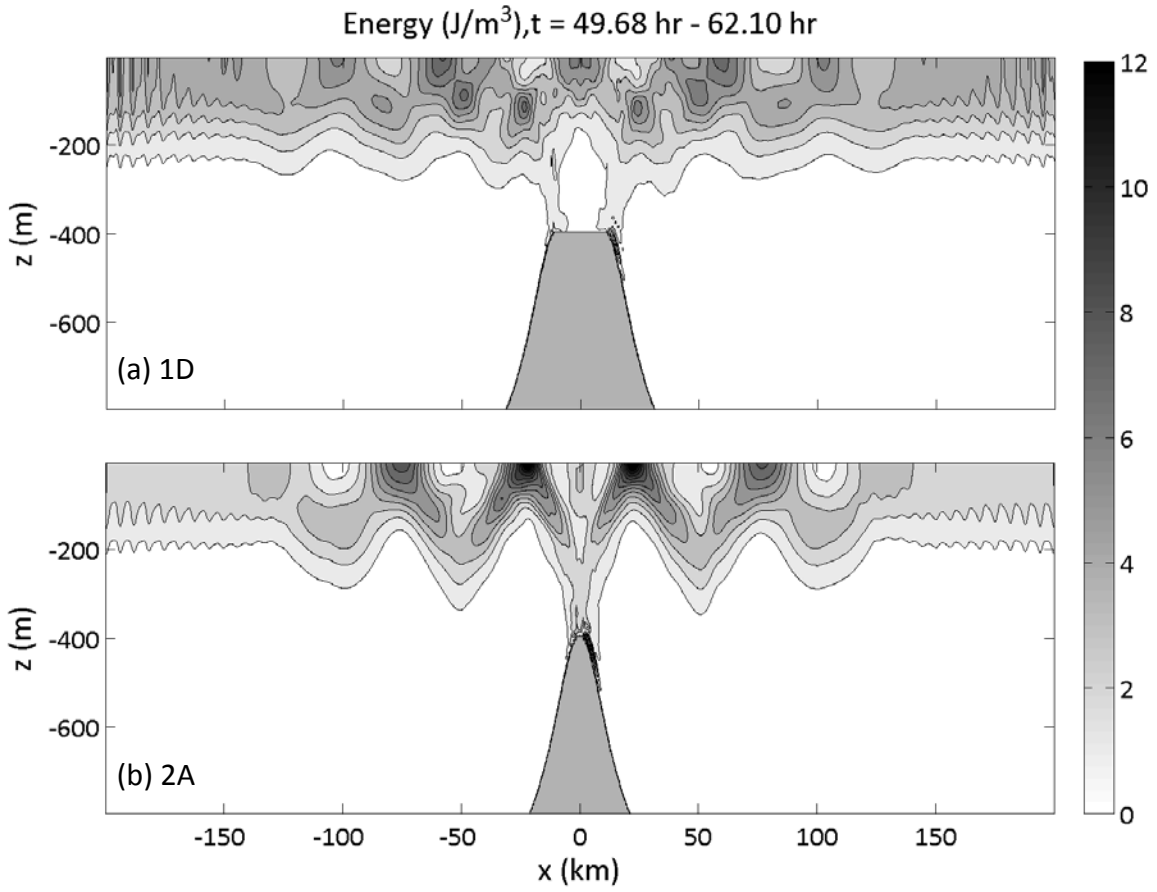


Figure 3.7. Internal wave energy density (J/m^3) for (a) 1D and (b) 2A averaged over one tidal cycle, 49.70 – 62.10 hours. The contour interval is 1 J/m^3

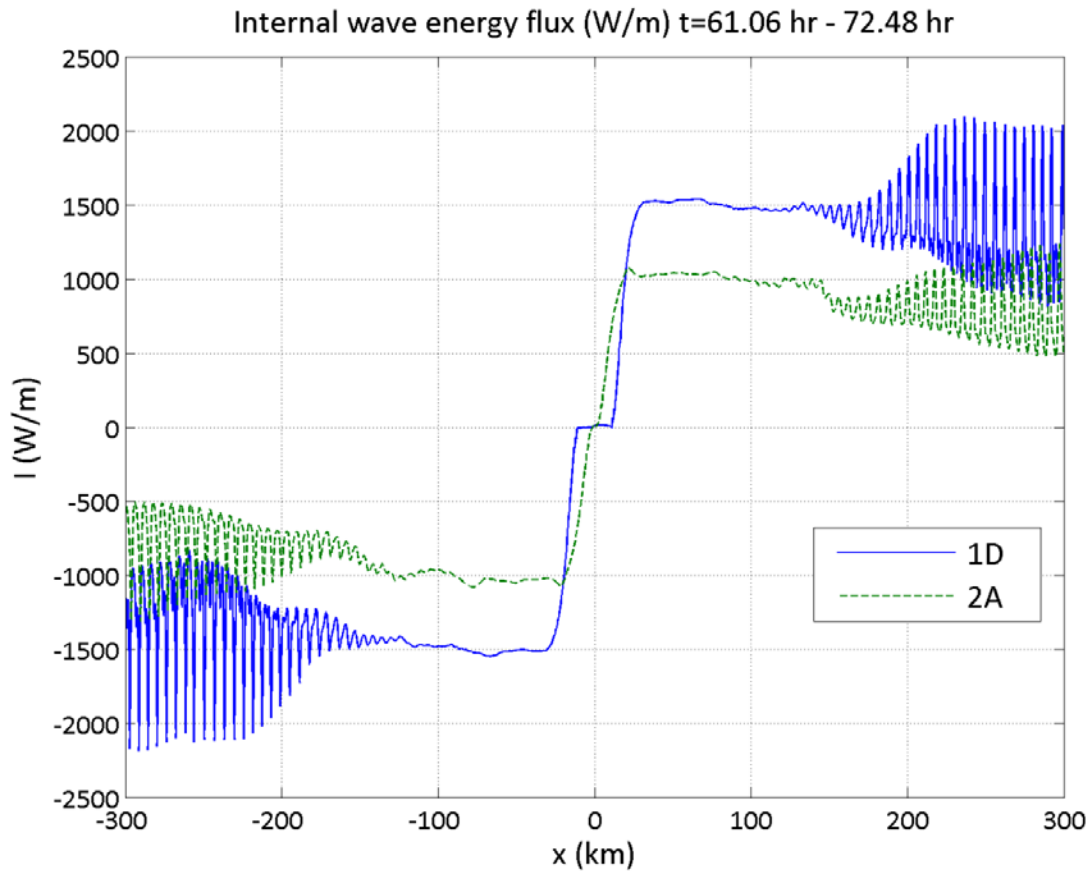


Figure 3.8. Vertically integrated horizontal energy flux (W/m) as a function of x for experiments 1D and experiment 2A. The flux is averaged over the tidal cycle 61.06 – 72.48 hours. The ridge is located at $x=0$ km

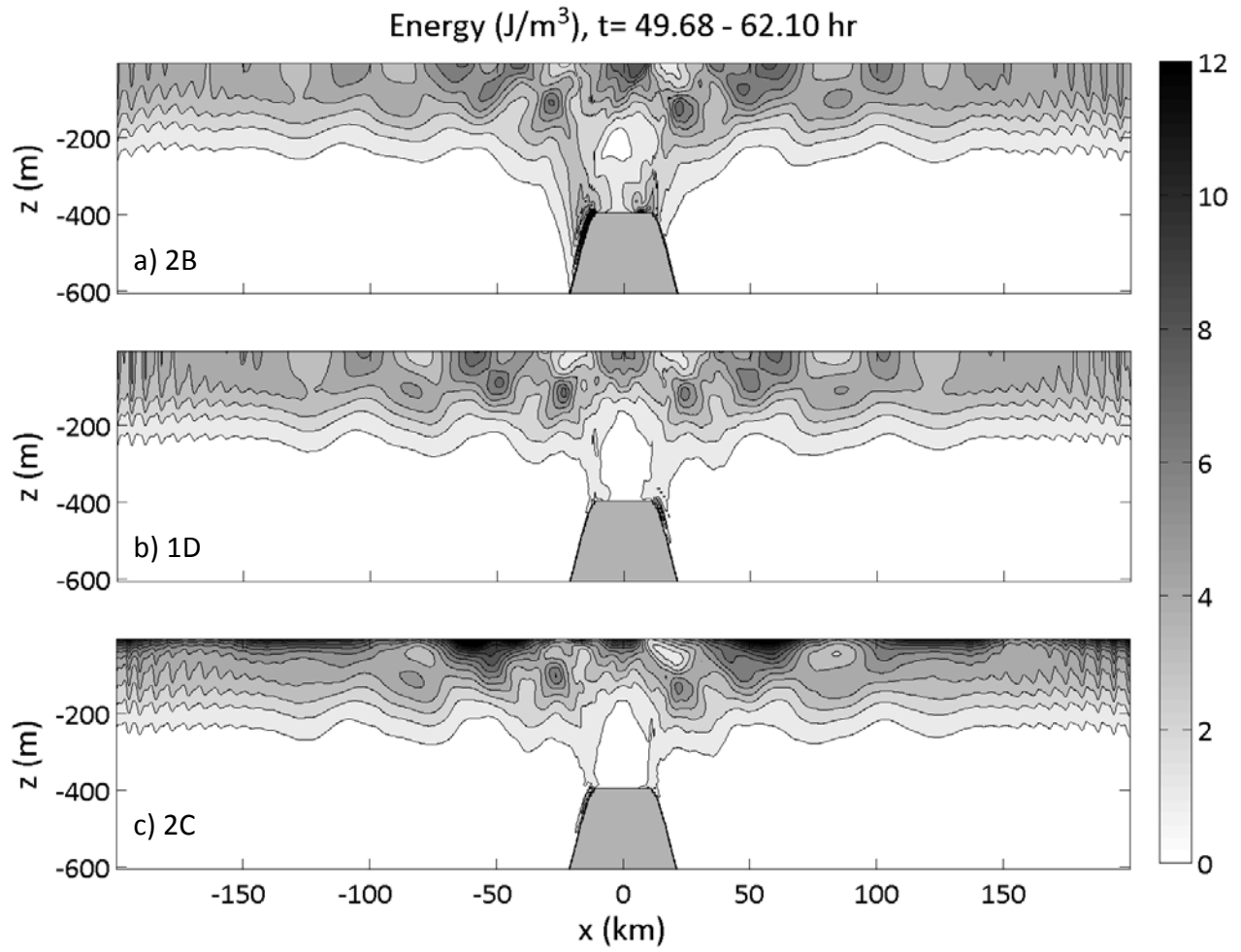


Figure 3.9 Internal wave energy density (J/m^3) for (a) 2B (b) 1D and (c) 2C. The energy density is averaged over one tidal cycle, 49.68 – 62.10 hours. The contour interval is 1 J/m^3

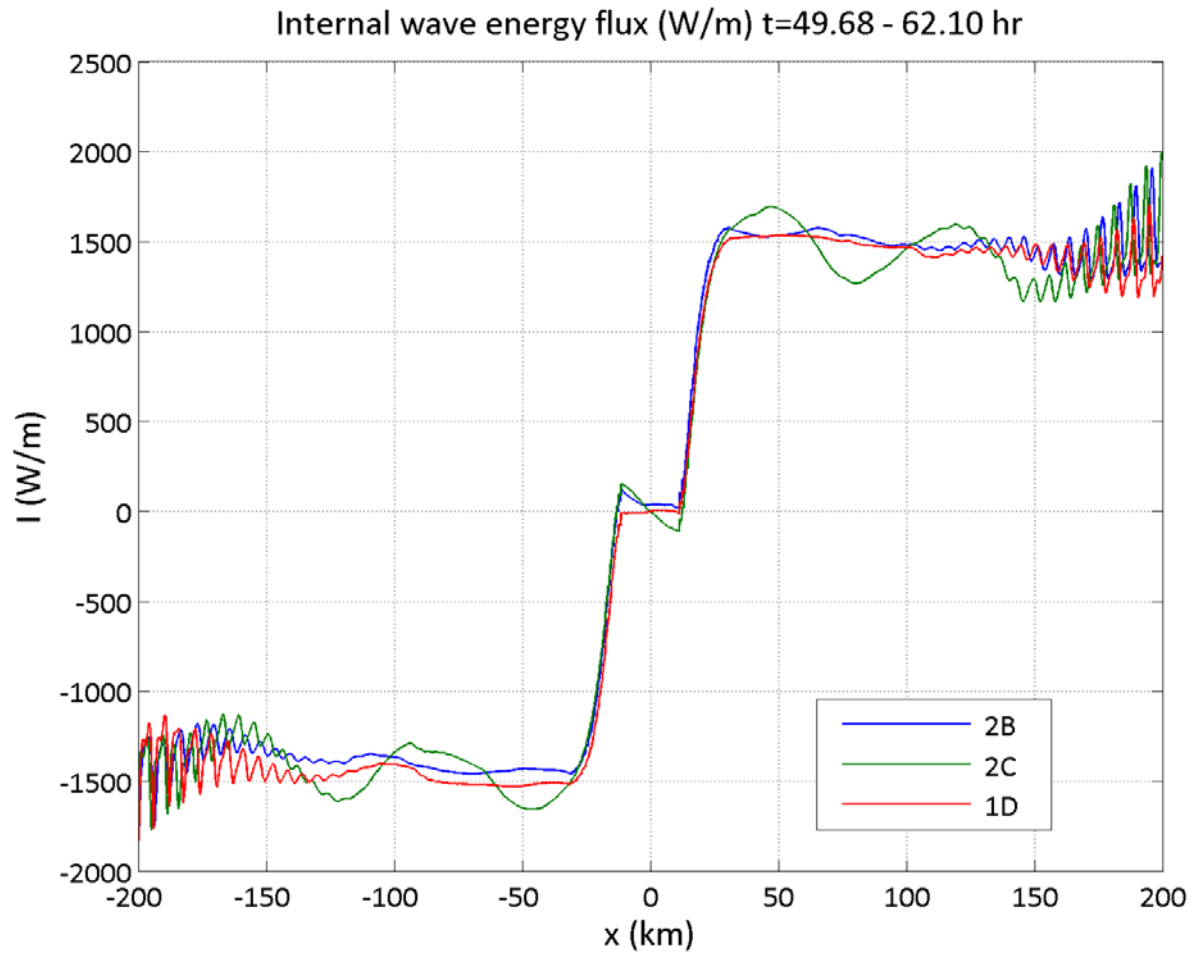


Figure 3.10. Vertically integrated horizontal energy flux (W/m) as a function of x for 1D forced by different tidal currents. The flux is averaged over the tidal cycle 49.68 – 62.10 hours. The ridge is located at $x=0$ km

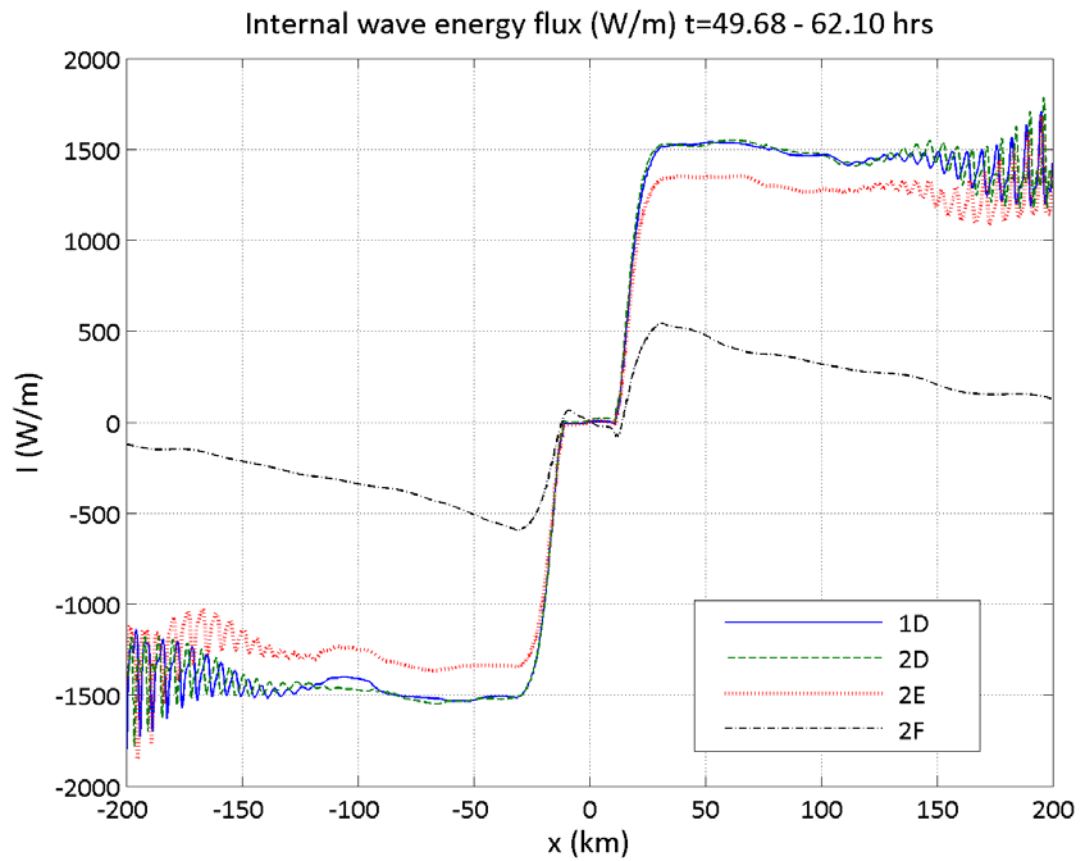


Figure 3.11. Vertically integrated horizontal energy flux (W/m) as a function of x at four different latitudes. The flux is averaged over the tidal cycle 49.68 – 62.10 hours. The ridge is located at $x=0$ km.

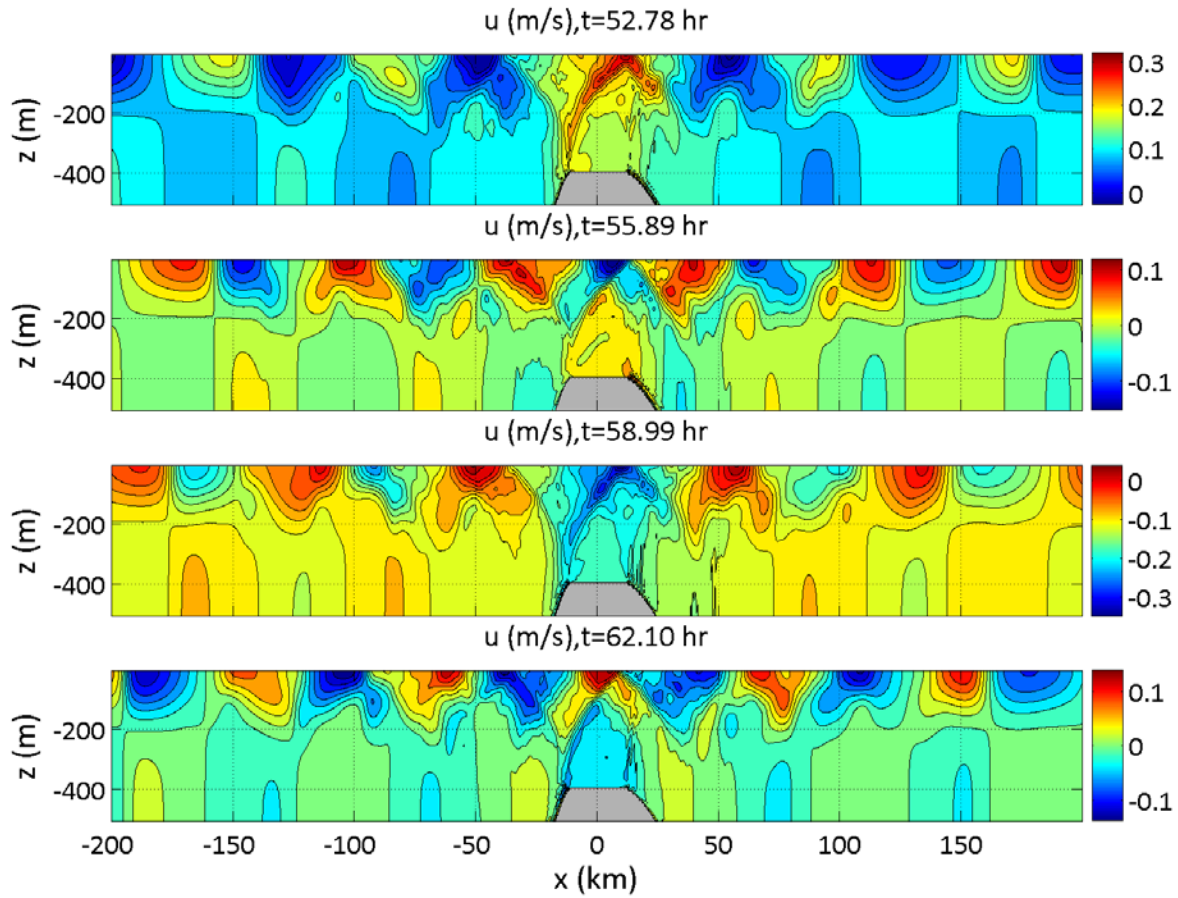


Figure 4.1. Contour plots of baroclinic velocity u in experiment 1G, at $t=52.78$ hours with increments every 3 hours. The barotropic tidal flow is at a maximum in the first and third panels (right and left respectively) and is zero in the second and fourth panels. The contour interval is 0.01m/s^{-1}

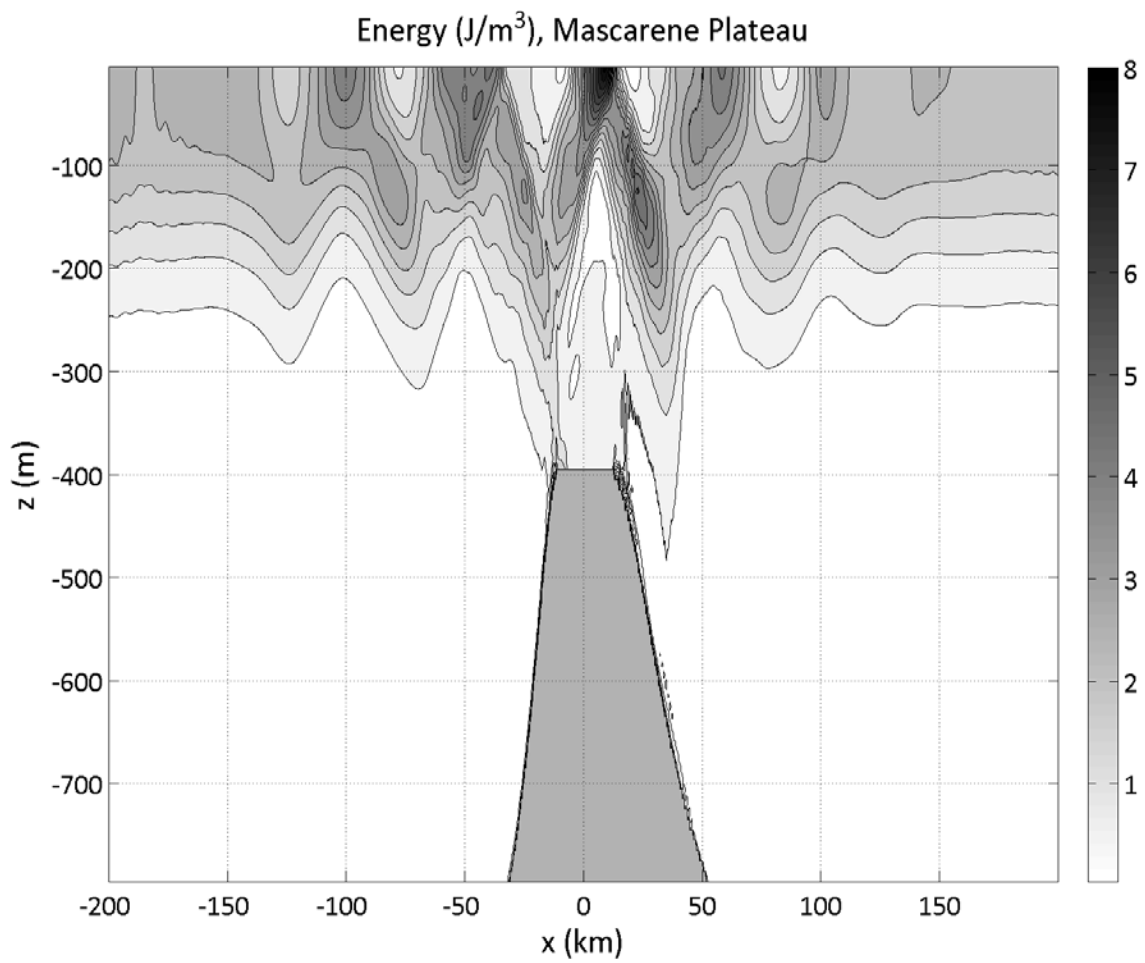


Figure 4.2. Internal wave energy density (J/m^3) for the Mascarene Plateau experiment 1G. Averaged over one tidal cycle, 48.65 – 60.97 hours. The contour interval is 0.5 J/m^3

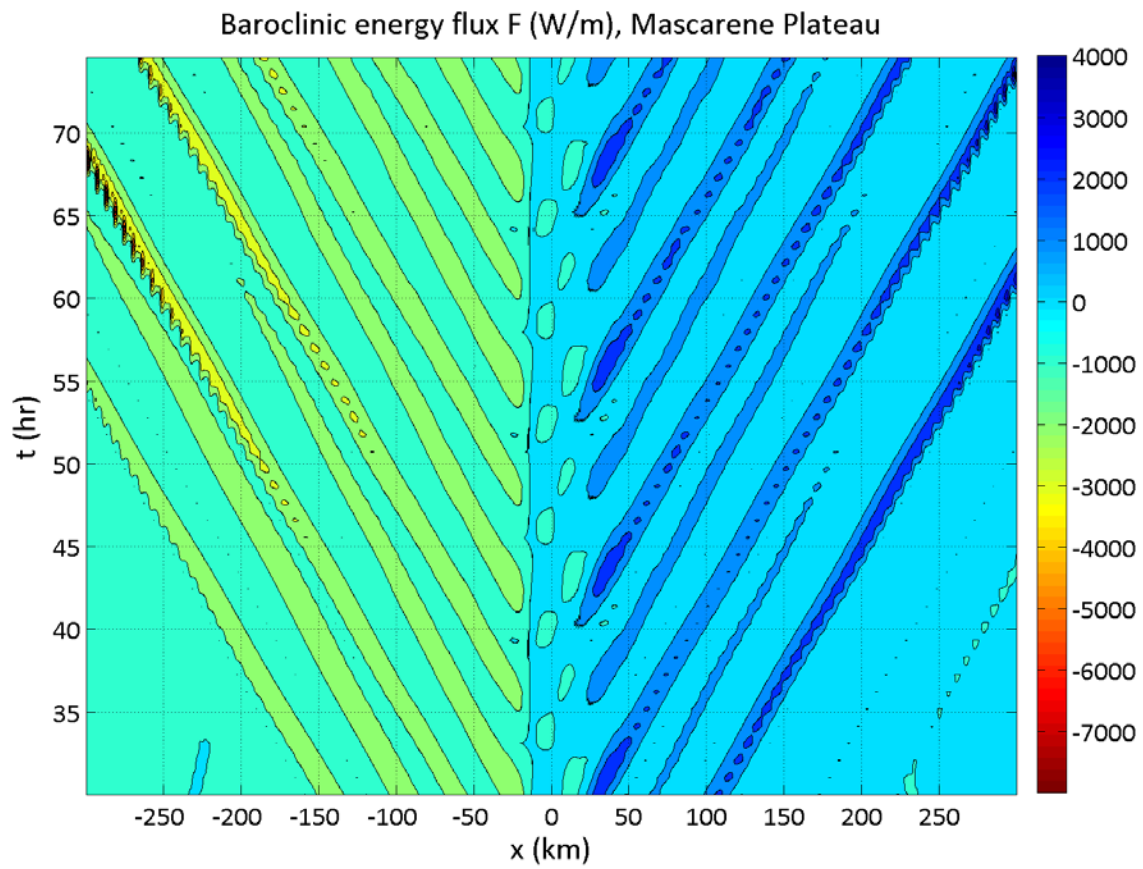


Figure 4.3. Vertically integrated energy flux in the x - t plane for the Mascarene plateau experiment 1G. Contour interval is 1000 (W/m)

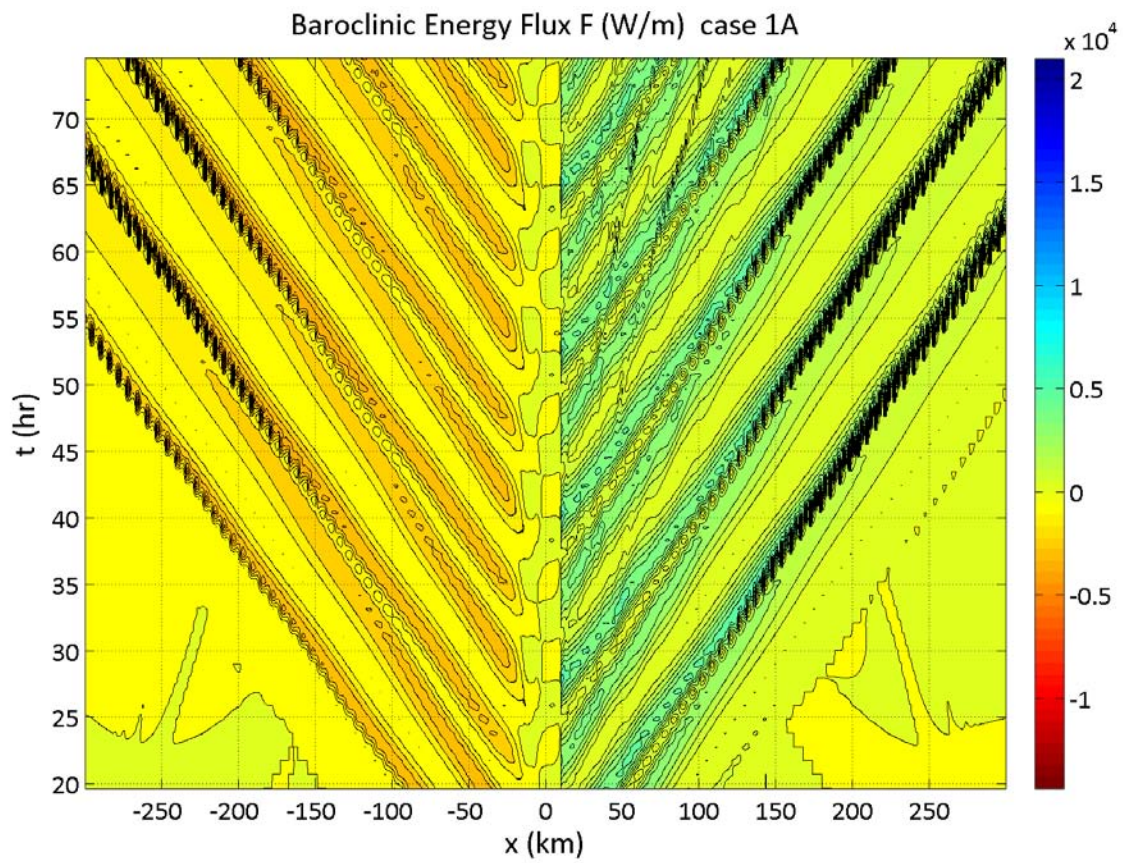


Figure 4.4. Vertically integrated energy flux in the x - t plane for experiment 1A, with a steep topography on the right side. Mode two waves are observed between $t=55$ and 70 hours in the region $x=0$ and 100 km. Contour interval is 750 (W/m)